INFORMATION TO USERS

This manuscript has been reproduced from the microfilm master. UMI films the text directly from the original or copy submitted. Thus, some thesis and dissertation copies are in typewriter face, while others may be from any type of computer printer.

The quality of this reproduction is dependent upon the quality of the copy submitted. Broken or indistinct print, colored or poor quality illustrations and photographs, print bleedthrough, substandard margins, and improper alignment can adversely affect reproduction.

In the unlikely event that the author did not send UMI a complete manuscript and there are missing pages, these will be noted. Also, if unauthorized copyright material had to be removed, a note will indicate the deletion.

Oversize materials (e.g., maps, drawings, charts) are reproduced by sectioning the original, beginning at the upper left-hand corner and continuing from left to right in equal sections with small overlaps.

Photographs included in the original manuscript have been reproduced xerographically in this copy. Higher quality 6" x 9" black and white photographic prints are available for any photographs or illustrations appearing in this copy for an additional charge. Contact UMI directly to order.

Bell & Howell Information and Learning
300 North Zeeb Road, Ann Arbor, MI 48106-1346 USA

UMI®
800-521-0600

Aerodynamic Inverse Design of Transonic Turbomachinery Cascades

Majid Ahmadi

A Thesis
in
The Department
of
Mechanical Engineering

Presented in Partial Fulfillment of the Requirements
For the Degree of Doctor of Philosophy
Concordia University
Montreal, Quebec, Canada

FEBRUARY 1998

National Library
of Canada

Acquisitions and
Bibliographic Services

395 Wellington Street
Ottawa ON K1A 0N4
Canada

Bibliothèque nationale
du Canada

Acquisitions et
services bibliographiques

395, rue Wellington
Ottawa ON K1A 0N4
Canada

Your file Votre référence

Our file Notre référence

0-612-40321-1

Canada

Abstract

Aerodynamic Inverse Design of Transonic Turbomachinery Cascades

Majid Ahmadi, Ph.D.
Concordia University, 1998

An aerodynamic inverse design method for turbomachinery cascades is presented and is implemented in a finite volume method. In this design method, the mass-averaged swirl schedule and the blade thickness distribution are prescribed. The design method then provides the blade shape that would accomplish this loading by imposing the appropriate pressure jump across the blades and satisfying the blade boundary condition, the latter implies that the flow is tangent to the blade surfaces. This inverse design method is implemented using a cell-vertex finite volume method which solves the Euler equations on unstructured triangular meshes. A five-stage Runge-Kutta pseudo-time integration scheme is used to march the solution to steady state. Non-linear artificial viscosity is added to eliminate

pressure-velocity decoupling and to capture shocks. Convergence is accelerated using local time stepping and implicit residual smoothing. The boundary conditions at inflow and outflow are based on the method of characteristics. The finite volume discretization method is validated against some standard cases of internal flow as well as linear cascades.

The inverse design method is first validated for three different cascades namely, a parabolic cascade, a compressor cascade and a turbine inlet guide vane. It is then used to obtain a shock-free design of an impulse transonic cascade and of the ONERA transonic compressor cascade. A parametric study has shown that the blade profile is rather sensitive to the prescribed loading distributions and that, in most cases, a smooth loading distribution results in a shock-free cascade design.

Acknowledgments

I would like to express my sincere gratitude and appreciation to my thesis supervisor, Professor Wahid S. Ghaly, for his continued guidance, support, enthusiasm and encouragement during the course of this research.

I would also like to thank Professor Georgios H. Vatistas for his support and guidance in the early stages of my Ph.D. program.

Special thanks are also due to all the personnel of CERCA (CEnter for Research on Computation and its Applications): the students, the technical staff, and the professors for the useful discussions, and the continued support and technical help in solving day-to-day problems, in particular, Dr. Dompierre for providing me with the mesh adaptation library LIBOM and Dr. Richer for his help with LaTeX. Without their help, this work would not have been possible.

The financial support of the National Science and Engineering Research Council of Canada, NSERC Grant #QGP0170337 and the Concordia University Faculty Research Development Program are gratefully acknowledged.

I would like to dedicate this thesis to the most important person in my life who shared with me both joys and pains and supported and encouraged me during the course of this study, to my beloved wife, Sheller.

Contents

List of Figures

Nomenclature

A_i	maximum eigenvalue of Euler equations
A, B	coefficients matrices
c	speed of sound
D	discretized AV integral
E	total internal energy per unit mass
F, G	flux vectors in the x- and y-directions, equation (2-2)
f	blade camber line, Figure 2-1, equation (2-20)
H	total enthalpy per unit mass
I_{xx}, I_{yy}, I_{xy}	second order moment
i, j, k	running index or unit Cartesian vectors
L	pseudo-Laplace operato.
M	Mach number

$\dot{m}$	mass flow rate
N, n	integer number or number of edges sharing a node
n_{x_e}, n_{y_e}	components of outward normal to an edge e
p_o	stagnation pressure
p	static pressure
Q	discretized flux integral
R_x, R_y	first order moment
R	residual or gas constant
(r, θ, z)	cylindrical coordinates
S_i	surface area of the cell i associated with node i
s	entropy or blade spacing-to-chord ratio, Figure 2-1
T_o	stagnation temperature
T	static temperature or matrix of eigenvector or blade thickness
t	time
U	vector of conservative variables
V	velocity vector
u, v	Cartesian velocity components

$\bar{v}$	mass-averaged velocity in the y-direction, also referred to as the tangential velocity
w	geometrical weight
x, y	Cartesian coordinates
α	flow angle or coefficients of multistage time stepping or defined in equation (2-13)
β	flow angle, Figure 2-1
γ	ratio of specific heats
δ, Δ	difference
ΔT	time-step
$\delta\Omega$	boundary of Ω
$\varepsilon_{ik}^{(2)}, \varepsilon_{ik}^{(4)}$	coefficients for 2nd and 4th order artificial viscosity terms
λ_x, λ_y	Cartesian coefficients
$\kappa^{(2)}, \kappa^{(4)}$	constants associated with artificial viscosity terms
ρ	density
ν	pressure switch
∇	gradient
Ω	volume of domain

Subscripts

e	edge index
i, k	nodal index
new	the new conservative values
old	the old time step of conservative values
old − avg	the old average values
p	primitive state vector
pred	the predicted values
spec	the specified values
bl	blade
LE	leading edge
max	maximum
o	stagnation condition
TE	trailing edge

Superscripts

(2), (4)	the second and fourth order

n	time level
$+$	blade upper side
$-$	blade lower side

Acronyms

AV	Artificial Viscosity
CFD	Computational Fluid Dynamics
CFL	Courant-Fredrick-Lewy number
FVM	Finite Volume Method
LIBOM	Library of Mesh Optimization

Chapter 1

Introduction

The flow in a turbomachine is typically three-dimensional, viscous and inherently unsteady. Figures 1-1 and 1-2 show the flow complexity in a compressor and turbine passage respectively, where schematic illustrations of several flow phenomena influencing performance are shown. The inherent unsteadiness is due to the series of fixed and rotating blade-rows. It is important to point out that only one case can be considered as steady (in the relative frame): it corresponds to the particular configuration of an isolated blade-row when the flow is attached and all the boundary conditions including a fixed rotational speed remain constant. In fact this case is very rare in a turbomachine: the unsteady effects can be neglected and the flow can be assumed as steady only in the first blade row of a compressor or turbine [2, 3].

There are many physical problems involving two-dimensional flows around blading

which remain unsolved. Figure 1-3 taken from Gostelow [1], shows a representative compressor blade and lists some of the unresolved problems. On the pressure surface the destabilizing effects of concave curvature usually result in Görtler vorticity. This affects the heat transfer and makes prediction of boundary layer characteristics difficult. Other problems are boundary layer transition and its inception, extent and behavior under free-stream turbulence, pressure gradients on concave surfaces. Separation is a related problem, especially the long and short bubble modes of laminar separation. Turbomachinery blading usually has a thick trailing edge, and the resulting trailing edge flows and base pressure cannot yet be reliably predicted. Unsteady interactions, especially the passage of wakes through blade rows, are complex phenomena that merit much closer attention. Solution of each of these problems requires a better understanding of the flow physics.

To understand the physics of the flow, mentioned above, numerous research activities using experimental as well as numerical approaches have been initiated in the past few decades. In order to improve the performance of modern highly loaded turbomachinery components, the designer needs a good understanding of the different flow phenomena occurring in a turbomachine passage. It is important to design aerodynamically efficient blade profiles. The viscous effects and shocks, for example, can be reduced by designing blade geometries which give a proper velocity (or pressure) distribution. In the past, this was done iteratively by successive modifications of the blade geometry followed by experimental verification or numerical flow simulation. However, depending on the designer

experience, such a process can be very time consuming, can result in increased design costs, moreover it may not always produce the targeted performance and usually does not result in break throughs in the technology.

A study of the published literature and of the present state-of-the-art shows that usually the detailed definition of the tubomachinery geometry is done iteratively using analysis code, which simulate inviscid or viscous flow namely Euler or Navier-Stokes solvers (this is referred to as the direct approach to the design). This process consists in choosing a blade geometry, and then analyzing the flow field around this geometry using analysis codes. If the target performance is not achieved, then a new blade geometry is guessed and the whole process is repeated, until the desired results are obtained, eventually. The task of guessing a blade geometry has been done in a great variety of ways. For example, it is common to use straight lines and circular arcs, or in general conic sections (such as elliptic arcs), both in the definition of the meridional geometry and of the camber surface (see Moore [4]). Another different form of doing this is presented in Baines *et al.*[5] who used Lamé ovals for the definition of the geometry of mixed flow turbines.

In what follows this approach, which is referred to as the analysis or direct method will be presented, it will be followed by a totally different approach, known as the inverse design method, where the blade performance is prescribed and the blade shape that would accomplish it is sought after as described below.

1.1 Analysis or Direct Approach

In the analysis method, a certain geometry is analyzed and, through the designer's experience, is modified to yield the required performance. Several analysis methods have been implemented to simulate inviscid and/or viscous flow in cascades. Among them, the Finite Volume Method (FVM) has proved to be simple yet very efficient in computing such flows. Also, this methodology is very suitable for approximating the solution in less cost and enough accuracy [6, 7, 8, 9, 10, 11, 12].

Over the last decade, there has been an increasing trend to use unstructured meshes (as opposed to structured ones) in discretizing the computational domain; the main advantages being: the ease of generating an isotropic mesh (using e.g. Delaunay triangulation) for an arbitrarily complex geometry without severely distorted mesh cells, and the fact that it couples naturally and efficiently with solution-adaptive schemes.

While Navier-Stokes solvers are needed to obtain accurate solutions for viscous flows in turbomachines, a fast Euler solver is still a desirable tool for routine applications particularly in problems where viscous effects are confined to the walls regions, typically in attached high Reynolds number subsonic flows. Many flow phenomena typical of turbomachines are present in two-dimensional cascades [1], therefore they provide a good test ground for the different numerical methods; a good compilation of these test cases can be found in Fottner [13].

In the blade-to-blade plane, or linear cascade, Arnone and Stecco [7] and Liu and Jameson [12] developed a cell-centered scheme to solve the Euler equations on a structured H-type mesh while Siden *et al.* [9] implemented a cell-vertex adaptive scheme using an unstructured triangular mesh where the entropy variation along the edges was used as an indicator for mesh refinement. More recently, Irmisch [14] presented a vertex-centered adaptive scheme where he used Delaunay triangulation to generate the mesh and to adapt it based on density variation along the edges.

Using cell vertex FVM, with linear approximation for all variables, global second-order accuracy can be achieved on unstructured meshes for the Euler equations [15]. It is found in practice that the solution accuracy is most significantly affected by mesh quality (smoothness, number of connections at a point), the construction of the artificial diffusion terms and the formulation of the inlet and outlet boundary conditions.

1.1.1 Present Analysis Approach

In the analysis mode of present study, inviscid flow in cascades is simulated by solving the Euler equations on purely triangular unstructured meshes using a time-marching solution method. The time dependent integral form of the equations are discretized in space using a cell-vertex Finite Volume Method (FVM) and integration in pseudo-time is performed using an explicit five-stage Runge-Kutta time-stepping procedure. Convergence acceleration is achieved by employing local time-stepping and implicit residual smoothing [16]. The

non-linear artificial viscosity formulation advanced by Jameson *et al.* [17, 6] combined with the pseudo-Laplacian discretization presented by Holmes and Connel [18] provide a model with lower numerical losses and higher accuracy. The inflow and outflow boundary conditions are based on a linearized one-dimensional characteristic method, developed by Giles [19, 20].

1.2 Inverse Design Method

The inverse design method is one where the required blade performance is specified and the blade shape that would accomplish such a performance is sought. Inverse techniques for turbomachine blades are widely used in industry, but they are far from being at the sophistication level of the analysis methods [8, 10, 11].

1.2.1 Previous Investigations

The first inverse design method was introduced by Lighthill [21] in 1945 for incompressible flow. He showed that one cannot prescribe any arbitrary velocity distribution in order to obtain a solution, but rather a given prescribed velocity distribution on the blade surface must satisfy certain constraints that deal 1) with the compatibility of the velocity distribution and the specified free-stream velocity and 2) with the closure of the profile. It has been shown that the same holds for compressible flow. Surface boundary layers can be taken into

account within the design procedure via any fast integral boundary layer computation [22]. The calculated displacement thickness is subtracted after smoothing from the computed profile to yield the final metal blade.

In two-dimensional blade-to-blade design methods, this performance is characterized with two design quantities: either the flow properties on both sides of the blade or the flow properties on one side (typically the suction side to eliminate possible shocks) and e.g. the blades thickness distribution. These flow properties may be either the pressure [22], the velocity [23], or the Mach number [24] distribution on the blades pressure and suction surfaces. These choices of the design variables are most appropriate for two-dimensional flow where the designer knows how to choose a 'good' pressure (or Mach number) distribution and where it is implicitly assumed that the two-dimensional plane under consideration is a stream-tube. However, in three-dimensional flow, the choice of a 'good' pressure distribution is unknown. Another choice of the design variables, that can readily be applied to the three-dimensional design problem, is the pressure jump across the blades and their thickness distribution. Novak and Haymann-Haber [25] and Zannetti [26] used these design variables for cascade design. Moreover Zannetti [26] extended his method to three-dimensional shock-free flows [3] and used it to design a subsonic stator.

A three-dimensional inverse blade design theory [27], referred to as the blade circulation method, was presented in 1984, where the arithmetic mean swirl distribution ($r\bar{v}_\theta(r, z)$ in cylindrical coordinates) is specified in the blade region and the blade shape that would

accomplish that swirl schedule is then calculated. A solution for a steady irrotational flow of an incompressible inviscid fluid over an infinitely thin blade set at zero incidence angle in a constant hub and shroud passage was given in the form of series of eigen functions [27]. That theory was further extended to handle complex passage geometry for incompressible [28] and compressible flow [29]; the numerical implementation involved the use of Fourier series in the circumferential direction and finite difference [28] or finite element [29] in the meridional plane (plane passing through the axis of the turbomachine) so that the three-dimensional problem was converted into a series of two-dimensional ones for the Fourier components. The method was also extended to handle transonic flow [30] and finite blade thickness [31] where a finite volume scheme in three dimensions was used to solve the flow equations. This is to list some of the research activities where this method has been applied.

Recently, this theory [27] has been modified such that the mass average, rather than the arithmetic average, swirl schedule is specified [32], the advantage being that the gradient of the mass-averaged swirl is directly proportional to the pressure jump across the blades (and the rate of change of angular momentum for a stator or specific work for a rotor), hence the Kutta condition can be directly and easily imposed, and the design method can be implemented into current Euler solvers. The specification of the mass-averaged swirl (which is directly proportional to the pressure jump across the blades) is more appropriate for three-dimensional flows as mentioned earlier, and the prescription of the blade thickness

guarantees that the profile is closed and gives the designer some control on structural and manufacturing constraints. As shown in [32], the finite volume Euler solver, which is based on Jameson's original cell-centered finite volume scheme [17] with blended second and fourth order nonlinear artificial diffusion, was used to demonstrate the effect of using the mass-averaged swirl as a design variable. This new design method has also been used to suggest some modifications to the three-dimensional aerodynamic blade design of a transonic fan [33].

1.2.2 Present Inverse Design Approach

In the present work, the inverse design method [32], where the design variables are the mass-averaged tangential velocity and the blades thickness distribution, is presented and is used to design the different compressor and turbine cascades. It is implemented in a cell-vertex finite volume method (FVM) on unstructured triangular meshes using an edge based data structure for efficient and optimum performance of the FVM [6, 15].

The advantage of prescribing the mass-averaged tangential velocity is that the gradient of the mass-averaged swirl is directly proportional to the pressure jump across the blades (and the rate of change of angular momentum), hence the Kutta condition can be directly and easily imposed, and the design method can be implemented into current Euler solvers. The specification of the mass-averaged swirl (which is directly proportional to the pressure

jump across the blades) is more appropriate for three-dimensional flows, and the prescription of the blade thickness guarantees that the profile is closed and gives the designer some control on structural and manufacturing constraints.

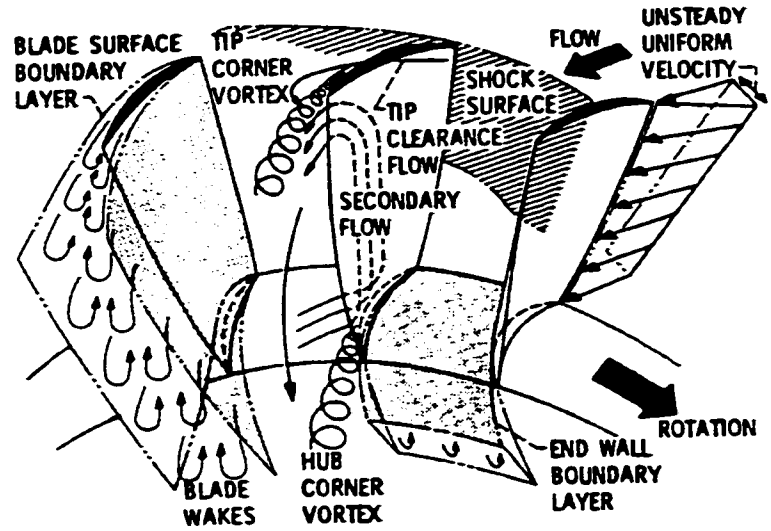

Figure 1-1: Compressor blade row: flow characteristics (Courtesy NASA-Lewis Research Center).

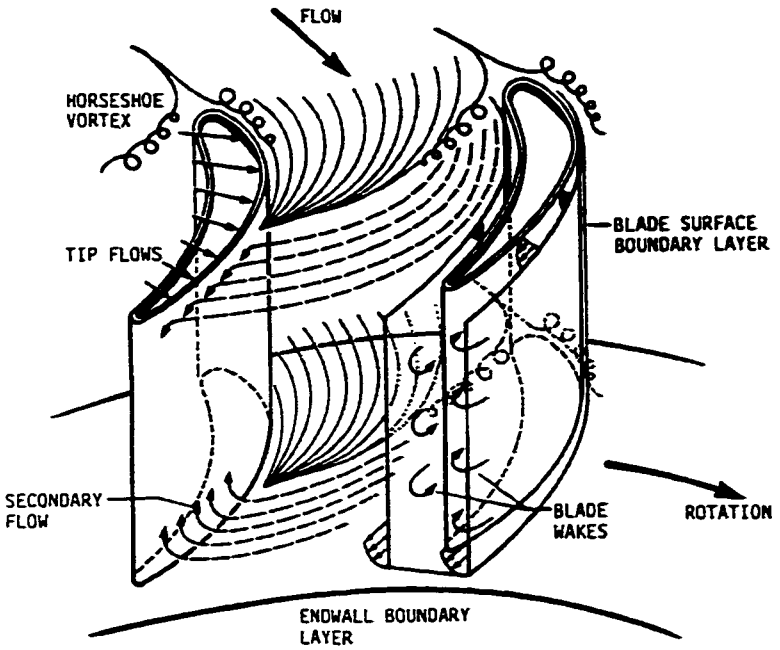

Figure 1-2: Turbine blade row: flow characteristics (Courtesy NASA-Lewis Research Center).

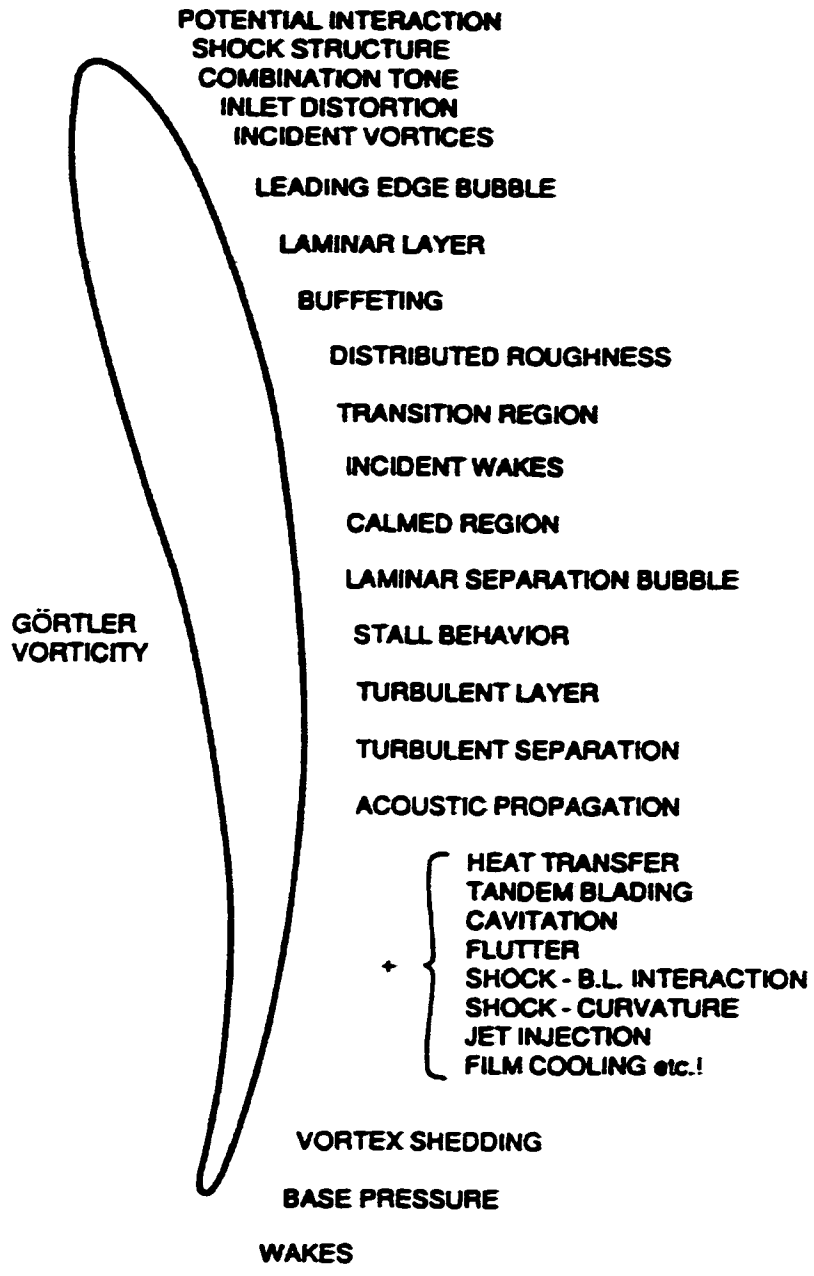

Figure 1-3: Some unresolved cascade flow problems, Gostelow [1].

Chapter 2

Inverse Design Methodology

In this chapter, the governing flow equations is first presented. Then, the inverse design method, where the design variables are the mass-averaged swirl schedule and the blades thickness distribution, is described. The blade boundary conditions and camber line equation are also explained.

2.1 Governing Equations

The continuity, momentum and energy equations, governing the unsteady two-dimensional flow of an inviscid fluid (loosely referred to as the Euler equations) are written in conservative form in a Cartesian coordinate system as follows:

$$\frac{\partial U}{\partial t} + \frac{\partial F}{\partial x} + \frac{\partial G}{\partial y} = 0 \qquad (2\text{-}1)$$

where U is a state vector of dependent variables and F and G are the flux vectors in the x and y directions, and are given by:

$$U = \begin{bmatrix} \rho \\ \rho u \\ \rho v \\ \rho E \end{bmatrix}, \quad F = \begin{bmatrix} \rho u \\ \rho u^2 + p \\ \rho uv \\ \rho uH \end{bmatrix}, \quad G = \begin{bmatrix} \rho v \\ \rho uv \\ \rho v^2 + p \\ \rho vH \end{bmatrix}. \tag{2-2}$$

Assuming that the fluid is an ideal gas thermally and calorically and, given the definition of total enthalpy H

$$H = E + p/\rho \tag{2-3}$$

the pressure p can then be written as:

$$p = (\gamma - 1)\,\rho \left[E - \frac{1}{2}\left(u^2 + v^2\right)\right] \tag{2-4}$$

where γ is the ratio of specific heats.

Additional equations which will be required are the definitions of the speed of sound, Mach number, stagnation pressure and stagnation temperature.

$$c = \sqrt{\frac{\gamma p}{\rho}} \tag{2-5}$$

$$M = \frac{\sqrt{u^2 + v^2}}{c} \tag{2-6}$$

$$p_o = p\left(1 + \frac{\gamma - 1}{2} M^2\right)^{\gamma/(\gamma-1)} \tag{2-7}$$

$$T_o = T\left(1 + \frac{\gamma - 1}{2} M^2\right) \tag{2-8}$$

In what follows, all distances are non-dimensionalized using an appropriate characteristic length and all flow variables are non-dimensionalized using the upstream stagnation pressure and temperature as follows:

$$p = \frac{p}{p_o}, \quad T = \frac{T}{T_o}, \quad u,v = \frac{u,v}{\sqrt{RT_o}}, \quad \rho = \frac{\rho}{p_o / RT_o}. \tag{2-9}$$

Since the Euler equations are nonlinear, they are solved iteratively using a time marching finite volume scheme that is discussed in detail in the next chapter.

2.2 Inverse Design Formulation

The inverse design method presented in [32] is summarized in this section, and the differences between that method and the current implementation are emphasized. In a linear cascade, the prescribed design quantities are the mass-averaged tangential velocity $\bar{v}(x)$ (which corresponds to the swirl schedule $r\bar{v}_\theta(r, z)$ in an annular cascade) and the blades thickness distribution $T(x)$. As mentioned earlier, the gradient of the mass-averaged swirl is directly proportional to the pressure jump across the blades. The specification of the blade thickness guarantees that the profile is closed and gives the designer some control over structural and manufacturing constraints.

The equations of motion, equations (2-1), are solved in both analysis and design modes, hence both modes are implemented in the same computer code, the primary difference comes in the implementation of the boundary conditions along the blades. In the analysis mode, the usual flow tangency condition is enforced; while in the design mode, the prescribed mass-averaged tangential velocity is used to impose a pressure jump across the blades and the blade boundary condition (implying that the flow be tangent to the blade surfaces) results in the imposition of the tangential component of velocity $v^{\pm}$ along the blade surfaces and the imposition of the camber line $f(x)$, as described hereafter.

2.2.1 The Mass-Averaged Swirl Schedule

Following the rectilinear cascade notation given in Figure 2-1, the mass-averaged tangential velocity $\bar{v}(x)$ in the bladed region is defined as [32]:

$$\bar{v}(x) = \frac{1}{\dot{m}} \int_{y^+}^{y^-} v(\rho u \, dy) \tag{2-10}$$

This velocity $\bar{v}(x)$ can be related to the local blade pressure loading via the y-momentum equation [32]:

$$\Delta p = p^+ - p^- = \dot{m} \frac{d\bar{v}}{dx} \tag{2-11}$$

where $\dot{m}$ is the mass flow rate through the blade passage, and the superscripts $(+)$ and $(-)$ denote the blade upper and lower surfaces, respectively. Equation (2-11) implies that

prescribing the pressure jump across the blades can be obtained by prescribing the mass-averaged tangential velocity, $\bar{v}(x)$ ($r\bar{v}_\theta(r,z)$ in an annular cascade). In the design mode, equation (2-11) is used to find pressure difference across the blade.

2.2.2 The Blade Boundary Conditions

The blade boundary condition implies that the flow is tangent to the blade surfaces, it can be expressed as [27]:

$$V^{\pm} \cdot \nabla \alpha^{\pm} = 0 \tag{2-12}$$

In the above expressions, the blade upper and lower surfaces are described by the constant surfaces $\alpha^{\pm}$ and are defined as [32]:

$$\alpha^{\pm} \equiv y - (f(x) \pm \frac{T(x)}{2}) = ns \tag{2-13}$$

where n is any integer, s is the blade spacing-to-chord ratio, $T(x)$ is the prescribed blade thickness distribution, and $f(x)$ is the unknown blade camber line in the inverse problem, as shown in Figure 2-1.

Subtracting and adding the two blade boundary conditions given in equations (2-12), we obtain:

$$(v^+ - v^-) = \left(u^+ - u^-\right)\frac{df}{dx} + \frac{1}{2}\left(u^+ + u^-\right)\frac{dT}{dx} \tag{2-14}$$

$$\left(u^+ + u^-\right)\frac{df}{dx} = (v^+ + v^-) - \frac{1}{2}\left(u^+ - u^-\right)\frac{dT}{dx} \tag{2-15}$$

Equations (2-14) and (2-15) are alternative forms of the flow tangency condition along the blades, referred to as the blade boundary condition in the inverse problem.

In the bladed region, fluid is allowed to cross the blade surfaces during the iterative process for the blade camber line, the technique used to satisfy the blade boundary conditions, equations (2-14) and (2-15) and the pressure loading, equation (2-11) is as follows. A blade value of a given quantity is defined as the average value of that quantity at the blade upper and lower surfaces, e.g. the blade value of the x-component of velocity is defined as:

$$\langle u \rangle_{\text{bl}} \equiv \frac{1}{2}\left[u^{+} + u^{-}\right] \tag{2-16}$$

and the difference between the blade upper- and lower-surface values is defined as:

$$\Delta_{\text{bl}}(u) = u^{+} - u^{-} \tag{2-17}$$

To satisfy the conditions given in equation (2-11) and equation (2-14), we enforce the following constraints on the pressure and the y-component velocity along the blade upper- and lower-surface:

$$v^{\pm} = \langle v \rangle_{\text{bl}} \pm \frac{1}{2}\left[\Delta_{\text{bl}}(u)\frac{df}{dx} + \langle u \rangle_{\text{bl}}\frac{dT}{dx}\right] \tag{2-18}$$

$$p^{\pm} = \langle p \rangle_{\text{bl}} \pm \frac{1}{2}\left[\dot{m}\frac{d\bar{v}}{dx}\right] \tag{2-19}$$

At convergence, the only contribution to the flux vectors on the blade surfaces are the pressure forces given in equation (2-11).

2.2.3 Camber Line Generator

In the design mode, the blade shape is periodically updated by integrating equation (2-15) (using the trapezoidal rule) from the blade leading to trailing edge [32]

$$f(x) = \int_0^x \left[\frac{\langle v \rangle_{\text{bl}}}{\langle u \rangle_{\text{bl}}} - \frac{1}{4} \frac{\Delta_{\text{bl}}(u)}{\langle u \rangle_{\text{bl}}} \frac{dT}{dx} \right] dx. \tag{2-20}$$

Each time the blade shape is updated, a new computational mesh needs to be generated. This can be implemented using either a sheared H-grid or a purely Delaunay triangular mesh as described in the next chapter.

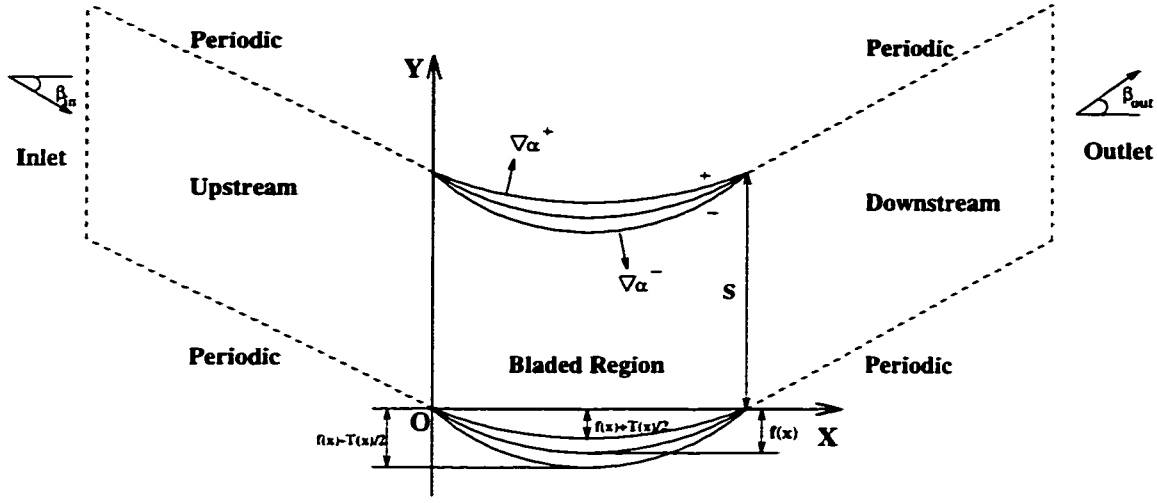

$$\alpha^{+}_{-} = y - (f(x) \pm T(x) / 2) = 0, S, 2S, 3S, ..., NS \quad \text{Blades}$$

Figure 2-1: Cascade notation and computational domain.

Chapter 3

Numerical Implementation

In this chapter, the finite volume discretization method and the boundary conditions implementation are first presented. Then, the numerical implementation of inverse design approach is described. The validation of finite volume solver and a mesh adaptation library used in optimizing the analysis mode are presented in appendix A.

3.1 Finite Volume Discretization Method

A cell-vertex finite volume method is used to discretize the equations of motion, equations (2-1), on an unstructured triangular mesh. The computational domain is divided into triangles, fixed in time, and the flow variables are stored at their vertices. For any node, the control volume (surface in 2D) is taken as the union of all triangles with a vertex at that node, i.e. the control volumes are overlapping.

The governing equations, equations (2-1), are then integrated over each control volume Ω (surface in 2D) which is bounded by the surface $\delta\Omega$ (curve in 2D), and using Gauss theorem (Green's Theorem in 2D) one obtains

$$\frac{\partial}{\partial t}\iint_{\Omega} U\,dx\,dy + \int_{\delta\Omega}(F dn_x + G dn_y) = 0. \tag{3-1}$$

The fluxes F and G along a particular edge of the control volume are numerically evaluated as the average of the nodal flux values at the ends of that edge, which assumes a linear variation along the control volume edges and is second order accurate [34].

When the cell-vertex discretization scheme is applied to equation (3-1), the following set of coupled ordinary differential equations is obtained for each cell or control volume i surrounding node i:

$$\frac{\partial}{\partial t}(S_i U_i) + \sum_{e=1}^{n}(F_e n_{x_e} + G_e n_{y_e}) = 0 \tag{3-2}$$

where the summation is taken over all edges of cell i, S_i is the cell area, U_i is the solution vector, F_e and G_e are the components of the flux vector on edge e, and n_{x_e}, n_{y_e} are the components of the outward normal to edge e. The fluxes F_e and G_e are functions of the flow variables at neighboring nodes, thus when equation (3-2) is written for all cells i, we get

$$\frac{\partial}{\partial t}(S_i U_i) + Q(U_i) = 0 \tag{3-3}$$

where the convective operator $Q(U_i)$ represents the discrete approximation to the convective flux integral. It should be mentioned that an edge-based data structure is used to

construct the connectivity of the unstructured mesh and the convective flux balance is computed in a single loop over the edges using indirect addressing.

3.2 Artificial Viscosity

Artificial viscosity terms are introduced to provide for pressure-velocity coupling, to capture shock waves and to diffuse non-physical numerical oscillations. The discretized Euler equations, equations (3-3) are augmented by an artificial viscosity term as follows.

$$\frac{\partial}{\partial t}\left(S_i U_i\right) + Q\left(U_i\right) - D\left(U_i\right) = 0 \tag{3-4}$$

where $D\left(U_i\right)$ represents the integral of the artificial viscosity term. $D\left(U_i\right)$ is formed of a blend of Laplacian and biharmonic terms [6]. The Laplacian is discretized using an undivided pseudo-Laplacian, proposed by Holmes and Connell [18], where an inexpensive approach using geometric weights is used

$$L\left(U_i\right) = \sum_{k=1}^{n} w_{k,i}\left(U_k - U_i\right). \tag{3-5}$$

where k represents all neighbors of node i. The weights $w_{k,i}$ are chosen such that the pseudo-Laplacian of a linear function will be zero, as would be the case for the true Laplacian. These weights $w_{k,i}$ are defined as

$$w_{k,i} = 1 + \Delta w_{k,i}. \tag{3-6}$$

Following Holmes and Connell [18], the $\Delta w_{k,i}$ are of the form

$$\Delta w_{k,i} = \lambda_{x,i}\left(x_k - x_i\right) + \lambda_{y,i}\left(y_k - y_i\right) \tag{3-7}$$

where

$$\lambda_{x,i} = \frac{\left(I_{xy}R_y - I_{yy}R_x\right)_i}{\left(I_{xx}I_{yy} - I_{xy}^2\right)_i}, \tag{3-8}$$

$$\lambda_{y,i} = \frac{\left(I_{xy}R_x - I_{xx}R_y\right)_i}{\left(I_{xx}I_{yy} - I_{xy}^2\right)_i} \tag{3-9}$$

and

$$R_{x,i} = \sum_{k=1}^{n}\left(x_k - x_i\right), \quad R_{y,i} = \sum_{k=1}^{n}\left(y_k - y_i\right), \tag{3-10}$$

$$I_{xx,i} = \sum_{k=1}^{n}\left(x_k - x_i\right)^2, \quad I_{yy,i} = \sum_{k=1}^{n}\left(y_k - y_i\right)^2, \tag{3-11}$$

$$I_{xy,i} = \sum_{k=1}^{n}\left(x_k - x_i\right)\left(y_k - y_i\right). \tag{3-12}$$

The Laplacian term at each node i is then constructed as:

$$\nabla^2 U_i = L\left(U_i\right) = \sum_{k=1}^{n} w_{k,i}\left(U_k - U_i\right) \tag{3-13}$$

The biharmonic AV term is formed by taking the pseudo-Laplacian of $\nabla^2 U$, which is done in a second loop over all edges

$$\nabla^4 U_i = \sum_{k=1}^{n}\left(\nabla^2 U_k - \nabla^2 U_i\right). \tag{3-14}$$

The final form of the artificial viscosity term at node i is

$$D\left(U_i\right) = \sum_{k=1}^{n}\left(\frac{A_k + A_i}{2}\right)\left[\varepsilon_{ik}^{(2)}\left(U_k - U_i\right) - \varepsilon_{ik}^{(4)}\left(\nabla^2 U_k - \nabla^2 U_i\right)\right] \tag{3-15}$$

where A_i is given [16]:

$$A_i = \sum_{e=1}^{n} |u_e n_{x_e} + v_e n_{y_e}| + c_e \sqrt{n_{x_e}^2 + n_{y_e}^2} \tag{3-16}$$

Physically, A_i represents the integral, over each cell i, of the maximum eigenvalue of the Euler equations ($|u| + c$) in the direction normal to each cell edge. By taking the average of A_i and A_k, the diffusion term becomes conservative in the U quantities.

To ensure that the AV is significant only in the vicinity of shocks and oscillations, the coefficients $\varepsilon_i^{(2)}$ and $\varepsilon_i^{(4)}$ are made proportional to the second derivative of the pressure and are defined as:

$$\varepsilon_{ik}^{(2)} = \kappa^{(2)} \max\left[\nu_i, \nu_k\right], \tag{3-17}$$

$$\varepsilon_{ik}^{(4)} = \max\left[0, \kappa^{(4)} - \varepsilon_{ik}^{(2)}\right] \tag{3-18}$$

where the pressure switch ν is given by:

$$\nu_i = \frac{\left|\sum_{k=1}^{n} w_{k,i}\,(p_k - p_i)\right|}{\sum_{k=1}^{n} (p_k + p_i)} \tag{3-19}$$

and $\kappa^{(2)}$ and $\kappa^{(4)}$ are empirical coefficients taken as $1/2$ and $1/128$ [16].

3.3 Time Integration

The space-discretized Euler equations, given in equations (3-4), are solved for the steady state solution by pseudo-time marching. Given some initial guess for the flow field, equations (3-4) become:

$$\frac{dU_i}{dt} + R(U_i) = 0, \quad i = 1, 2, 3, \ldots \tag{3-20}$$

where $R(U_i)$ is the residual

$$R(U_i) = \frac{1}{S_i}\left[Q(U_i) - D(U_i)\right]. \tag{3-21}$$

These equations are integrated in time using a fully explicit five-stage hybrid time-stepping Runge-Kutta scheme, where the convective flux operator $Q(U_i)$ is evaluated at each stage in the time step, and the AV term $D(U_i)$ is evaluated only in the first two stages, and is then frozen at that value. The solution is advanced one time step Δt as follows:

$$\begin{aligned}
U_i^{(0)} &= U_i^n, \\
U_i^{(1)} &= U_i^{(0)} - \alpha_1 \frac{\Delta t_i}{S_i}\left[Q\left(U_i^{(0)}\right) - D\left(U_i^{(0)}\right)\right], \\
U_i^{(2)} &= U_i^{(0)} - \alpha_2 \frac{\Delta t_i}{S_i}\left[Q\left(U_i^{(1)}\right) - D\left(U_i^{(1)}\right)\right], \\
U_i^{(3)} &= U_i^{(0)} - \alpha_3 \frac{\Delta t_i}{S_i}\left[Q\left(U_i^{(2)}\right) - D\left(U_i^{(1)}\right)\right], \\
U_i^{(4)} &= U_i^{(0)} - \alpha_4 \frac{\Delta t_i}{S_i}\left[Q\left(U_i^{(3)}\right) - D\left(U_i^{(1)}\right)\right], \\
U_i^{(5)} &= U_i^{(0)} - \alpha_5 \frac{\Delta t_i}{S_i}\left[Q\left(U_i^{(4)}\right) - D\left(U_i^{(1)}\right)\right], \\
U_i^{n+1} &= U_i^{(5)}
\end{aligned} \tag{3-22}$$

where U_i^n and U_i^{n+1} are the values at the beginning and at the end of the n^{th} time step and the coefficients $\alpha's$ are:

$$\alpha_1 = \frac{1}{4}, \quad \alpha_2 = \frac{1}{6}, \quad \alpha_3 = \frac{3}{8}, \quad \alpha_4 = \frac{1}{2}, \quad \alpha_5 = 1. \tag{3-23}$$

This scheme represents a particular case of a large class of hybrid time-stepping schemes, which have been specifically designed to produce strong damping characteristics of the high-frequency error modes.

3.4 Convergence Acceleration

To accelerate the convergence to steady state, local time stepping and implicit residual smoothing have been implemented.

3.4.1 Local Time Stepping

The local time step for each cell i is set to the maximum stable value and is given by:

$$\Delta t_i = \mathrm{CFL}\frac{S_i}{A_i} \tag{3-24}$$

where CFL is Courant-Fredrick-Lewy number and A_i is defined by equation (3-16).

3.4.2 Implicit Residual Smoothing

The residual R_i at node i is implicitly smoothed by replacing it by an average of the residuals at the neighboring nodes [16]:

$$\bar{R}_i = R_i + \epsilon \nabla^2 \bar{R}_i \tag{3-25}$$

where ϵ is a smoothing coefficient. The Laplacian term $\nabla^2 \bar{R}_i$ is computed by a looping over all the edges using the pseudo-Laplacian formulation and the geometrical weights so that equation (3-25) may be written as:

$$\bar{R}_i = \frac{R_i + \epsilon \sum_{j=1}^{n} w_{j,i} \bar{R}_j}{1 + \epsilon \sum_{j=1}^{n} w_{j,i}} \tag{3-26}$$

Since the resulting matrix of residuals is diagonally-dominant for the ϵ values of interest, this implicit system can be solved by performing several Jacobi iterations:

$$\bar{R}_i^{(m)} = \frac{R_i^{(0)} + \epsilon \sum_{j=1}^{n} w_{j,i} \bar{R}_j^{(m-1)}}{1 + \epsilon \sum_{j=1}^{n} w_{j,i}} \tag{3-27}$$

where $R_i^{(0)}$ represents the unsmoothed residual. In practice only two iterations were used to get an adequate approximation of the smoothed residual. This smoothing technique allows the CFL number in equation (3-24) to be increased up to values of 8 or even higher.

3.5 Inflow and Outflow Boundary Conditions

The computation of inflow and outflow boundary conditions is based upon a linearized one-dimensional characteristic method, described in Giles [19, 20] and Lindquist [34]. At each inflow/outflow boundary there is a certain number of incoming/outgoing modes. The changes in the outgoing characteristic values are taken from the changes predicted by the flow solver. The changes in the incoming characteristics are determined such as to satisfy specified boundary conditions. The flow angles, stagnation enthalpy and stagnation pressure are specified at inflow, while the static pressure is specified at outflow.

This approach is based upon a characteristic analysis of the linearized Euler equations. At each inflow or outflow boundary there is a certain number of incoming modes and a certain number of outgoing ones. The first step in the process is to linearize the Euler equations (2-1). Using equation (2-2) to eliminate E from equations (2-1), and rearranging substantially, yields the following primitive form of the Euler equations.

$$\frac{\partial}{\partial t}\begin{pmatrix}\rho\\ u\\ v\\ p\end{pmatrix}+\begin{pmatrix}u & \rho & 0 & 0\\ 0 & u & 0 & \frac{1}{\rho}\\ 0 & 0 & u & 0\\ 0 & \gamma p & 0 & u\end{pmatrix}\frac{\partial}{\partial x}\begin{pmatrix}\rho\\ u\\ v\\ p\end{pmatrix}+\begin{pmatrix}v & \rho & \rho & 0\\ 0 & v & 0 & 0\\ 0 & 0 & v & \frac{1}{\rho}\\ 0 & 0 & \gamma p & v\end{pmatrix}\frac{\partial}{\partial y}\begin{pmatrix}\rho\\ u\\ v\\ p\end{pmatrix}=0 \quad \text{(3-28)}$$

This equation is still nonlinear. The next step is to consider small perturbations from a uniform, steady flow, and neglect all but the first order linear terms. This produces a linear

equation of the following form where the spatial directions x and y are along the grid lines.

$$\frac{\partial U_p}{\partial t} + A\frac{\partial U_p}{\partial x} + B\frac{\partial U_p}{\partial y} = 0 \tag{3-29}$$

where U_p is the primitive state vector variables

$$U_p = \begin{bmatrix} \rho \\ u \\ v \\ p \end{bmatrix} \tag{3-30}$$

and the coefficient matrices A and B are constant matrices based on the uniform, steady variables

$$A = \begin{pmatrix} u & \rho & 0 & 0 \\ 0 & u & 0 & \frac{1}{\rho} \\ 0 & 0 & u & 0 \\ 0 & \gamma p & 0 & u \end{pmatrix}, \quad B = \begin{pmatrix} v & \rho & \rho & 0 \\ 0 & v & 0 & 0 \\ 0 & 0 & v & \frac{1}{\rho} \\ 0 & 0 & \gamma p & v \end{pmatrix} \tag{3-31}$$

It is clear that a number of approximation errors are being introduced in converting the nonlinear Euler equations into the linearized equations. For steady state calculations the error will be proportional to the square of the steady state perturbation at the inflow and outflow. These should be very small and may well be unnoticeable except for the case of an oblique shock at the outflow.

Because the wave propagation normal to the boundary is dominant, variations parallel to the boundary may be neglected and the linearized one-dimensional Euler equations, in

primitive variables, can be written as:

$$\frac{\partial U_p}{\partial t} + A\frac{\partial U_p}{\partial x} = 0 \tag{3-32}$$

The reference state for evaluating the matrix A will be the state on the boundary at the old time step. To make the matrix A constant, the average value of the state vector on the boundary will be used to evaluate A. This state will be denoted by the subscript $()_{old-avg}$. Then, the constant matrix A is

$$A = \begin{pmatrix} u & \rho & 0 & 0 \\ 0 & u & 0 & \frac{1}{\rho} \\ 0 & 0 & u & 0 \\ 0 & \rho c^2 & 0 & u \end{pmatrix}_{old-avg} \tag{3-33}$$

where equation (2-5) is used. The matrix A can be diagonalized by a similarity transformation,

$$T^{-1}AT = \begin{bmatrix} u & 0 & 0 & 0 \\ 0 & u & 0 & 0 \\ 0 & 0 & u+c & 0 \\ 0 & 0 & 0 & u+c \end{bmatrix}_{old-avg} = \Lambda \tag{3-34}$$

where the matrix T is the matrix of right eigenvectors of A and the matrix $T^{-1}$is the matrix of left eigenvectors of A. Matrix Λ is a diagonal matrix whose elements are the eigenvalues

of matrix A.

$$T = \begin{pmatrix} \frac{-1}{c^2} & 0 & \frac{1}{2c^2} & \frac{1}{2c^2} \\ 0 & 0 & \frac{1}{2\rho c} & \frac{-1}{2\rho c} \\ 0 & \frac{1}{\rho c} & 0 & 0 \\ 0 & 0 & \frac{1}{2} & \frac{1}{2} \end{pmatrix}_{old-avg} , \; T^{-1} = \begin{pmatrix} -c^2 & 0 & 0 & 1 \\ 0 & 0 & \rho c & 0 \\ 0 & \rho c & 0 & 1 \\ 0 & -\rho c & 0 & 1 \end{pmatrix}_{old-avg} \tag{3-35}$$

Multiplication of equation (3-32) by T^{-1} produces the equation

$$\frac{\partial \phi}{\partial t} + \Lambda \frac{\partial \phi}{\partial x} = 0 \tag{3-36}$$

where $\phi = T^{-1}U_p$. Variation from the values at the old time step will be considered, therefore $\delta\phi = T^{-1}\delta U_p$. The four equations in the system of equations (3-36) are now independent. The elements of ϕ are the linearized characteristic variables and the corresponding elements of Λ indicate the direction of the flow of information. For subsonic flow where $0 < u < c$ the first three characteristics gives waves propagating downstream since the corresponding elements of Λ are positive and the fourth propagating upstream since the fourth element of Λ is negative. For supersonic flow where $u > c$ all waves propagate downstream since all elements of Λ are positive.

3.5.1 Subsonic Inflow Boundary

For subsonic inflow, there are three incoming waves and one outgoing wave. The outgoing characteristic wave is obtained from the flow solver whereas the three incoming waves are

specified by prescribing the values of total enthalpy H, entropy s, and flow angle α

$$H = \left(\frac{\gamma}{\gamma - 1}\right)\frac{p}{\rho} + \frac{1}{2}\left(u^2 + v^2\right) \tag{3-37}$$

$$s = \ln(p) - \gamma \ln(\rho) \tag{3-38}$$

$$\tan\alpha = v/u \tag{3-39}$$

Note that specifying the total enthalpy H and entropy s is equivalent to specifying the total temperature and pressure. A numerical boundary condition or outgoing characteristic wave predicted by flow solver is denoted by the subscript $()_{\text{pred}}$. Let also the subscript $()_{\text{spec}}$ stand for the value which is specified by the inlet flow conditions and the subscripts $()_{\text{old}}$ and $()_{\text{new}}$ for the values at the old and new time steps. The amount needed to bring the old values of H, s and $\tan\alpha$ on the boundary to the specified values can be written in terms of a first order Taylor series in ϕ. The constant coefficient of the series can be changed by using the chain rule to contain elements of U_p. Using relation $U_p = T\,\phi$,

$$\begin{aligned}
(H)_{\text{spec}} &= (H)_{\text{new}} \\
&= (H)_{\text{old}} + \left(\frac{\partial H}{\partial \phi}\right)_{\text{old-avg}} \delta\phi \\
&= (H)_{old} + \left(\frac{\partial H}{\partial U_p}\right)_{\text{old-avg}} \left(\frac{\partial U_p}{\partial \phi}\right)_{\text{old-avg}} \delta\phi \\
&= (H)_{\text{old}} + \left(\frac{\partial H}{\partial U_p}\right)_{\text{old-avg}} T_{\text{old-avg}} \quad \delta\phi \\
&= (H)_{\text{old}} + \left[\begin{array}{cccc} \dfrac{1}{(\gamma-1)\,\rho} & \dfrac{v}{\rho c} & \dfrac{c+u}{2\rho c} & \dfrac{c-u}{2\rho c} \end{array}\right]_{\text{old-avg}} \delta\phi
\end{aligned} \tag{3-40}$$

$$\begin{aligned}(s)_{\text{spec}} &= (s)_{\text{old}} + \left(\frac{\partial s}{\partial U_p}\right)_{\text{old-avg}} T_{\text{old-avg}} \quad \delta\phi \\ &= (s)_{\text{old}} + \begin{bmatrix} \frac{1}{p} & 0 & 0 & 0 \end{bmatrix}_{\text{old-avg}} \delta\phi \end{aligned} \tag{3-41}$$

$$\begin{aligned}(\tan\alpha)_{\text{spec}} &= (\tan\alpha)_{\text{old}} + \left(\frac{\partial \tan\alpha}{\partial U_p}\right)_{\text{old-avg}} T_{\text{old-avg}} \quad \delta\phi \\ &= (\tan\alpha)_{\text{old}} + \begin{bmatrix} 0 & \frac{1}{\rho u c} & \frac{-v}{2\rho u^2 c} & \frac{v}{2\rho u^2 c} \end{bmatrix}_{\text{old-avg}} \delta\phi \end{aligned} \tag{3-42}$$

The change in the fourth characteristic $\delta(\phi_4)$ is equal to the change that the flow field predicts, $\delta(\phi_4)_{\text{pred}}$. Since $\delta\phi = T^{-1}\delta U_p$, the predicted change in the characteristic variable $\delta(\phi_4)_{\text{pred}}$ is found to be

$$\delta(\phi_4)_{pred} = (-\rho c)_{\text{old}}\, \delta u_{\text{pred}} + \delta p_{\text{pred}} \tag{3-43}$$

there are now four equations for the change in the characteristic variable ϕ which can be written in matrix form

$$\begin{bmatrix} (H)_{\text{spec}} - (H)_{\text{old}} \\ (s)_{\text{spec}} - (s)_{\text{old}} \\ (\tan\alpha)_{\text{spec}} - (\tan\alpha)\,\text{old} \\ \delta(\phi_4)_{\text{pred}} \end{bmatrix} = \begin{bmatrix} \frac{1}{(\gamma-1)\rho} & \frac{v}{\rho c} & \frac{c+u}{2\rho c} & \frac{c-u}{2\rho c} \\ \frac{1}{p} & 0 & 0 & 0 \\ 0 & \frac{1}{\rho u c} & \frac{-v}{2\rho u^2 c} & \frac{v}{2\rho u^2 c} \\ 0 & 0 & 0 & 1 \end{bmatrix}_{\text{old-avg}} \begin{bmatrix} \delta(\phi_1) \\ \delta(\phi_2) \\ \delta(\phi_3) \\ \delta(\phi_4) \end{bmatrix} \tag{3-44}$$

Using the relation $\delta U_p = T\,\delta\phi$, $\delta\phi$ in equation (3-44) can now be changed back into

primitive state vector values U_p

$$\delta U_p = \begin{bmatrix} \delta(\rho) \\ \delta(u) \\ \delta(v) \\ \delta(p) \end{bmatrix}_{new}$$

$$= \frac{1}{uc+u^2+v^2} \begin{bmatrix} \frac{\rho u}{c} & \frac{-p}{c}\left(\frac{\gamma u}{\gamma-1}+\frac{u^2+v^2}{c^2}\right) & \left(\frac{-\rho v}{c}\right)u^2 & \frac{u^2+v^2}{c^2} \\ u & \frac{-up}{(\gamma-1)\rho} & (-v)\,u^2 & \frac{-u}{\rho} \\ v & \frac{-vp}{(\gamma-1)\rho} & (c+u)\,u^2 & \frac{-v}{\rho} \\ \rho c u & \frac{-cup}{(\gamma-1)} & (-\rho c v)\,u^2 & u^2+v^2 \end{bmatrix}_{old-avg}$$

$$\times \begin{bmatrix} (H)_{\text{spec}} - (H)_{\text{old}} \\ (s)_{\text{spec}} - (s)_{\text{old}} \\ (\tan\alpha)_{\text{spec}} - (\tan\alpha)_{\text{old}} \\ \delta(\phi_4)_{\text{pred}} \end{bmatrix}. \quad (3\text{-}45)$$

To transform the change in the primitive state vector variables δU_p back into the change in the state vector δU the following transformation is performed,

$$\delta U_{\text{new}} = \begin{bmatrix} \delta(\rho) \\ \delta(\rho u) \\ \delta(\rho v) \\ \delta(\rho E) \end{bmatrix}_{\text{new}} = \begin{bmatrix} 1 & 0 & 0 & 0 \\ u & \rho & 0 & 0 \\ v & 0 & \rho & 0 \\ \frac{1}{2}(u^2+v^2) & \rho u & \rho v & \frac{1}{\gamma-1} \end{bmatrix}_{\text{new}} \begin{bmatrix} \delta(\rho) \\ \delta(u) \\ \delta(v) \\ \delta(p) \end{bmatrix}_{\text{new}} \quad (3\text{-}46)$$

Hence, the change in the conservative variables at inlet becomes:

$$\delta U_{\text{new}} = \begin{bmatrix} \delta(\rho) \\ \delta(\rho u) \\ \delta(\rho v) \\ \delta(\rho E) \end{bmatrix} = M_1 \times \frac{M_2}{uc + u^2 + v^2} \times M_3 \tag{3-47}$$

where

$$M_1 = \begin{bmatrix} 1 & 0 & 0 & 0 \\ u & \rho & 0 & 0 \\ v & 0 & \rho & 0 \\ (u^2+v^2)/2 & \rho u & \rho v & 1/\gamma - 1 \end{bmatrix}_{\text{new}}, \quad M_2 = \begin{bmatrix} \frac{\rho u}{c} & M_2^{1,2} & \left(\frac{-\rho v}{c}\right) u^2 & \frac{u^2+v^2}{c^2} \\ u & \frac{-up}{(\gamma-1)\rho} & (-v)\,u^2 & \frac{-u}{\rho} \\ v & \frac{-vp}{(\gamma-1)\rho} & (c+u)\,u^2 & \frac{-v}{\rho} \\ \rho c u & \frac{-cup}{(\gamma-1)} & (-\rho c v)\,u^2 & u^2+v^2 \end{bmatrix}_{\text{old-avg}},$$

$$M_3 = \begin{bmatrix} (H)_{\text{spec}} - (H)_{\text{old}} \\ (s)_{\text{spec}} - (s)_{\text{old}} \\ (\tan\alpha)_{\text{spec}} - (\tan\alpha)_{\text{old}} \\ (-\rho c)_{\text{old}}\,\delta u_{\text{pred}} + \delta p_{\text{pred}} \end{bmatrix}, \qquad M_2^{1,2} = \frac{-p}{c}\left(\frac{\gamma u}{\gamma - 1} + \frac{u^2+v^2}{c^2}\right)$$

Using the equation (3-47), the new value of the state vector U at the inlet nodes becomes

$$U_{\text{new}} = U_{\text{old}} + \delta U_{\text{new}}. \tag{3-48}$$

3.5.2 Subsonic Outflow Boundary

For subsonic outflow, three outgoing waves are calculated from the numerical solution, while the incoming wave is fixed by specifying the static back pressure, p_{back}. Once again the amount needed to bring the old value of p to the specified value on the boundary can be written in terms of a first order Taylor series in ϕ

$$\begin{aligned}
(p)_{\text{spec}} &= (p)_{\text{new}} \\
&= (p)_{\text{old}} + \left(\frac{\partial p}{\partial \phi}\right)_{\text{old-avg}} \delta\phi \\
&= (p)_{\text{old}} + \left(\frac{\partial p}{\partial U_p}\right)_{\text{old-avg}} \left(\frac{\partial U_p}{\partial \phi}\right)_{\text{old-avg}} \delta\phi \\
&= (p)_{old} + \left(\frac{\partial p}{\partial U_p}\right)_{\text{old-avg}} T_{\text{old-avg}} \quad \delta\phi \\
&= (p)_{\text{old}} + \left[\begin{array}{cccc} 0 & 0 & \frac{1}{2} & \frac{1}{2} \end{array}\right]_{\text{old-avg}} \delta\phi.
\end{aligned} \tag{3-49}$$

The change in the first, second and third characteristics is equal to the change the flow field predicts. Again, since $\delta\phi = T^{-1}\delta U_p$, the predicted change in the characteristic variables $\delta(\phi_1)_{\text{pred}}$, $\delta(\phi_2)_{\text{pred}}$ and $\delta(\phi_3)_{\text{pred}}$ are found to be

$$\delta(\phi_1)_{\text{pred}} = \left(-c^2\right)_{\text{old}} \delta\rho_{pred} + \delta p_{\text{pred}} \tag{3-50}$$

$$\delta(\phi_2)_{\text{pred}} = (\rho c)_{\text{old}} \delta v_{\text{pred}} \tag{3-51}$$

$$\delta(\phi_3)_{\text{pred}} = (\rho c)_{\text{old}} \delta u_{\text{pred}} + \delta p_{\text{pred}} \tag{3-52}$$

As in the subsonic inlet condition, there are now four equations for the change in the characteristic variable ϕ

$$\begin{bmatrix} \delta(\phi_1)_{\text{pred}} \\ \delta(\phi_2)_{\text{pred}} \\ \delta(\phi_3)_{\text{pred}} \\ (p)_{\text{spec}} - (p)_{\text{old}} \end{bmatrix} = \begin{bmatrix} 1 & 0 & 0 & 0 \\ 0 & 1 & 0 & 0 \\ 0 & 0 & 1 & 0 \\ 0 & 0 & \frac{1}{2} & \frac{1}{2} \end{bmatrix}_{old-avg} \begin{bmatrix} \delta(\phi_1) \\ \delta(\phi_2) \\ \delta(\phi_3) \\ \delta(\phi_4) \end{bmatrix}. \tag{3-53}$$

Using the relation $\delta U_p = T\,\delta\phi$, $\delta\phi$ in equation (3-53) can now be changed back into primitive state vector values U_p

$$\begin{aligned} \delta U_p &= \begin{bmatrix} \delta(\rho) \\ \delta(u) \\ \delta(v) \\ \delta(p) \end{bmatrix}_{\text{new}} \\ &= \begin{bmatrix} \frac{-1}{c^2} & 0 & 0 & \frac{-1}{c^2} \\ 0 & 0 & \frac{1}{\rho c} & \frac{-1}{\rho c} \\ 0 & \frac{1}{\rho c} & 0 & 0 \\ 0 & 0 & 0 & 1 \end{bmatrix}_{\text{old-avg}} \begin{bmatrix} (-c^2)_{\text{old}}\ \delta\rho_{\text{pred}} + \delta p_{\text{pred}} \\ (\rho c)_{old}\ \delta v_{\text{pred}} \\ (\rho c)_{\text{old}}\ \delta u_{\text{pred}} + \delta p_{\text{pred}} \\ (p)_{\text{spec}} - (p)_{\text{old}} \end{bmatrix} \end{aligned} \tag{3-54}$$

The primitive state vector variables, δU_p, are transformed to the state vector, δU, by equation (3-46). Hence the corresponding change in values of the conservative variables at the

outlet nodes becomes:

$$\delta U_{\text{new}} = \begin{bmatrix} \frac{-1}{c^2} & 0 & 0 & \frac{-1}{c^2} \\ 0 & 0 & \frac{1}{\rho c} & \frac{-1}{\rho c} \\ 0 & \frac{1}{\rho c} & 0 & 0 \\ 0 & 0 & 0 & 1 \end{bmatrix}_{\text{old-avg}} \times \begin{bmatrix} (-c^2)_{\text{old}}\ \delta\rho_{\text{pred}} + \delta p_{\text{pred}} \\ (\rho c)_{\text{old}}\ \delta v_{\text{pred}} \\ (\rho c)_{\text{old}}\ \delta u_{\text{pred}} + \delta p_{\text{pred}} \\ (p)_{\text{spec}} - (p)_{\text{old}} \end{bmatrix} \tag{3-55}$$

The update is performed as in equation (3-48).

3.5.3 Supersonic Inflow Boundary

There are four incoming waves for supersonic inflow which can be specified by inlet Mach number $(M)_{\text{spec}}$, the inflow angle $(\alpha)_{\text{spec}}$, and subsequently the flow condition will be determined from these variables using isentropic relations.

3.5.4 Supersonic Outflow Boundary

There are four outgoing waves for supersonic outflow which can be predicted by numerical solution. Therefore the change in the state vector predicted by the scheme is used

$$\delta U_{\text{new}} = \delta U_{\text{pred}}. \tag{3-56}$$

3.6 Periodic Boundary Conditions

For a linear cascade, the flow periodicity implies that all the variables are the same at periodic pairs of nodes. To avoid interpolation and the accompanying inaccuracy, the grid generation provides the periodic nodes in pairs. To implement the periodicity condition, these pairs of periodic nodes are treated as interior nodes by adding all the contributions at any one periodic node to its periodic pair.

3.7 Wall Boundary Conditions

The wall boundary conditions are implemented in different manner for analysis and design approaches.

3.7.1 Analysis Approach

For an inviscid flow along an impermeable wall, the flow tangency condition implies that all fluxes through the wall faces vanish except for the pressure contribution to the momentum flux. However, since the flux through any edge on the wall is the average of the two nodal fluxes associated with that edge, it is possible that the average flux vanishes while the nodal fluxes do not. For this reason, it was found necessary to explicitly impose the tangency condition.

By imposing tangency at these nodes, this oscillatory state cannot occur and the change in the state vector is such that the new conservative variables will satisfy flow tangency on the boundary. At each wall node a flow angle, α, is prescribed. The second and third conservative variables are changed from the value predicted by solver, denoted by the subscript $()_{\text{RK-stage}}$, so the new values become:

$$(\rho u)_{\text{new}} = (\rho u)_{\text{RK-stage}} + (\rho w)_n \sin\alpha \tag{3-57}$$

$$(\rho v)_{\text{new}} = (\rho v)_{\text{RK-stage}} - (\rho w)_n \cos\alpha \tag{3-58}$$

where

$$(\rho w)_n = -(\rho u)_{\text{RK-stage}} \sin\alpha + (\rho v)_{\text{RK-stage}} \cos\alpha. \tag{3-59}$$

3.7.2 Design Approach

In the design approach, the flow tangency condition is expressed in terms of $p^{\pm}$ and $v^{\pm}$ as given in equations (2-18) and (2-19). These values of p and v are used at the beginning of each time step, together with ρ and ρu, to compute a new set of conservative variables along the blade surfaces; two of these variables, namely ρu and ρv, are fixed during each Runge-Kutta stage. Note that, during the iterations, there will be flow through the blades.

In other words, both design and analysis approaches use a Dirichlet boundary condition on the mass flux components, ρu and ρv. In the analysis approach, these components are modified to satisfy the flow tangency condition described in the previous section whereas,

in the design approach, the conservative variables are updated such that $p^{\pm}$ satisfies the global y-momentum equation (2-19) and $v^{\pm}$ satisfies the blade boundary condition, equations (2-18).

3.8 Inverse Design Implementation

As explained in chapter 2, the analysis and design modes are implemented in the same computer code, which solves the Euler equations using a cell-vertex finite volume method, where Euler equations are integrated in pseudo-time to steady state; the only difference between both modes is in the boundary conditions imposed along the blade surfaces.

When running in the analysis mode, the tangency condition along the blade surfaces is imposed at each pseudo-time step as described above either implicitly, by imposing zero fluxes through the control volume edges coinciding with the blade surfaces, or explicitly as described in § 3.7 to avoid velocity decoupling since a zero average flux can result from two non-zero equal fluxes but of opposite signs.

In the design mode, given some initial guess for the blade camber line $f(x)$ as described below, the Euler equations are marched in pseudo-time for m iterations then the following steps are executed periodically every n pseudo-time iterations:

1. A new blade shape $f(x)$ is computed from equation (2-20) and is relaxed (an under-relaxation factor of about 0.2 is typically used).

2. The mesh between the blade leading edge and the outflow planes is shifted in the y-direction by the amount of change occurring in the camber line $f(x)$ as described in the following section.

3. Using the latest blade shape $f(x)$ and the prescribed blade thickness, a new value for $v^{\pm}$ and $p^{\pm}$ is computed from equations (2-18) and (2-19) and is used at the beginning of each time step, together with ρ and ρu, to compute a new set of conservative variables along the blade surfaces; two of these variables, namely ρu and ρv, are fixed during each Runge-Kutta stage.

The above-mentioned iteration procedure is continued until convergence, which is measured by the L2-norm of the residual of the equations of motion, is reached.

In the design mode, it was found that, for the test cases presented in this work, the iteration procedure is rather insensitive to the initial guess of the camber line $f(x)$, for convenience a parabolic profile that is tangent to the inlet and exit flow angles is taken as an initial guess for $f(x)$. For convenience also, the flow regions upstream and downstream of the blades are usually constructed so as to be parallel to the inflow and outflow directions, which are prescribed in the design approach. Last but not least, note that this design method is a fully inverse method: given the design choices which are the mass-average tangential velocity $\bar{v}(x)$ and the blades thickness $T(x)$, the design iteration described above can be executed until convergence, without any special procedure at the start of (or during) the design iterations.

3.8.1 Grid Remeshing

In this work, sheared H-grids and Delaunay triangular meshes have been used to discritize the computational domain. Figures 3-1, 3-2 and 3-3 show these two types of meshes and a close-up view of the leading edge area of an inlet guide vane cascade with round LE and TE. As it is shown in these figures, the Delaunay triangular mesh is unaffected by the presence of a fat round leading edge whereas the sheared H-grid is highly distorted near the LE and, if the mesh is further refined, this distortion will increase resulting in more numerical error in that crucial area. The following sections explain the remeshing procedure for these two types of meshes.

3.8.1.1 Remeshing of Sheared H-grid Triangular Meshes

An unstructured mesh generator has been developed to construct an sheared H-mesh. The advantage of such a mesh is the ease of generating it and, more importantly, the remeshing is almost trivial as discussed below. The triangular mesh is produced by cutting quadrilateral into two triangles based on the minimum area of each triangle or minimum angle between two edges of each triangle. In this mesh generator, two hyperbolic type stretching functions are also used to provide clustering for mesh points in the x- and y-directions [35]. During the design iteration process, as the blade camber line $f(x)$ is changing, the x-coordinate is fixed, while the y-coordinate, between the leading edge and the exit planes, is displaced by the amount of change occurring in the camber line $f(x)$.

3.8.1.2 Remeshing of Delaunay Triangular Meshes

For Delaunay triangular meshes, the remeshing procedure is more elaborate. Normally, the number of nodes on the pressure and suction sides of the blade is not equal and also the nodes are not at the same x-location. Since equations (2-18) and (2-19) require the computation of Δv and Δp across the blades, it was decided to have nodes on opposite sides of the blade added or moved to the same x-location to avoid interpolation and the associated error. This is implemented in a pre-processing step.

Two different approaches have been developed to carry out the remeshing process. The first approach is to use an elliptic solver or smoothing process (spring analogy) to move the mesh-points due to movement of the camber line $f(x)$. During the design iteration process, since the blade camber line $f(x)$ is changing, the mesh-points are moved accordingly to new locations using the smoothing process and, if the mesh is not regular enough, the triangle edges maybe swapped.

The second approach is to use transfinite interpolation. During the design iteration process, as the blade camber line $f(x)$ is changing, the new value of the y-coordinate at each node in the bladed and downstream regions is computed using linear interpolation while the x-coordinate remains the same.

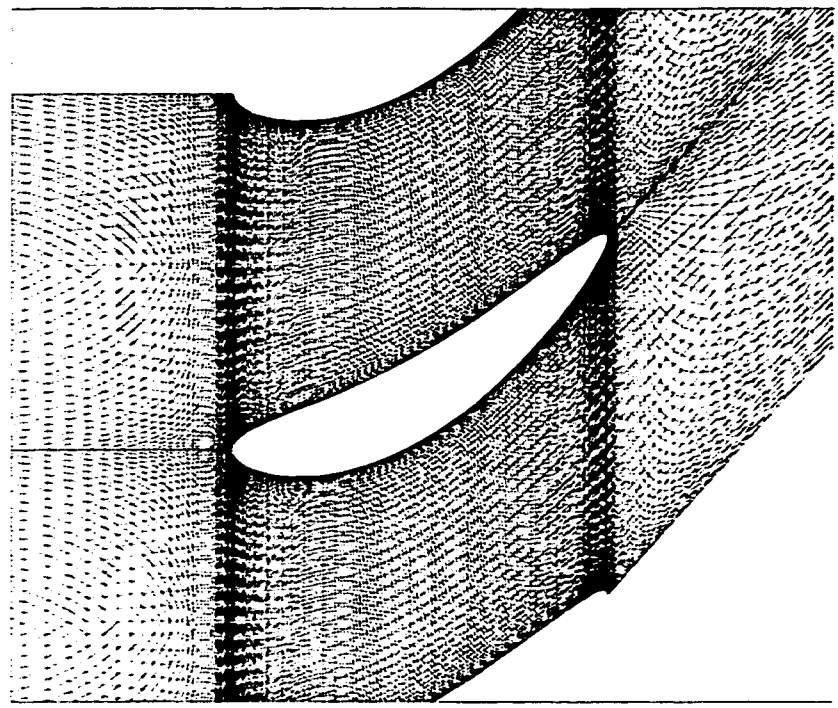

Figure 3-1: Unstructured triangular sheared H-mesh for an inlet guide vane cascade.

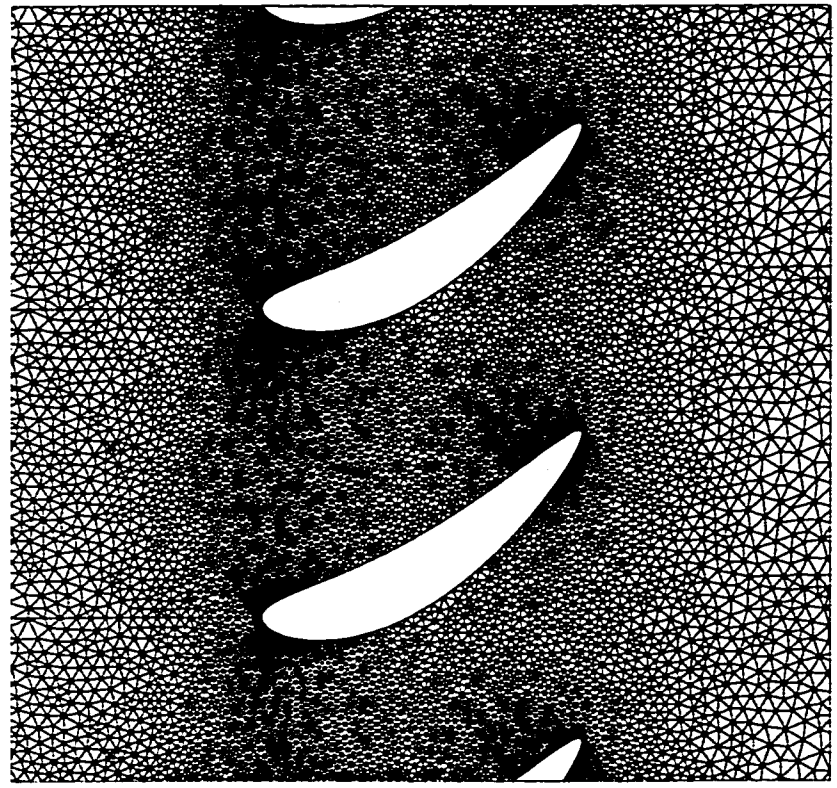

Figure 3-2: Unstructured Delaunay triangular mesh for an inlet guide vane cascade.

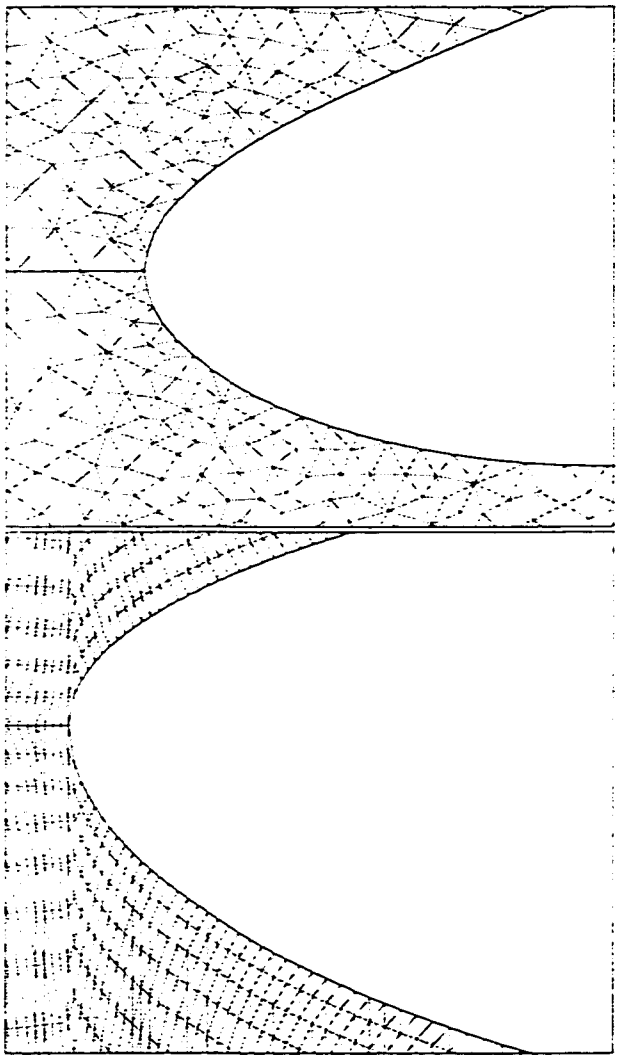

Figure 3-3: Unstructured Delaunay and sheared H-mesh with a close-up view of leading edge area of an inlet guide vane cascade.

Chapter 4

Inverse Design Results

In this chapter, the design method described in chapter 2 is first validated for three different cascades namely, parabolic cascade, compressor cascade and turbine inlet guide vane. The usefulness of the inverse design method in eliminating shocks is then demonstrated on the design of an impulse transonic cascade and on the redesign of the ONERA transonic compressor cascade [13]. A parametric study is performed to demonstrate the effect of the different prescribed loading distributions on blade profile and on the incidence angle. A sensitivity study of the effect of the initial camber profile on the convergence history is also carried out.

It should be mentioned that each pair of cases, compared hereafter, accomplishes the same overall change in mass-averaged tangential velocity, i.e. each pair accomplishes the same amount of overall turning (or change in angular momentum). For demonstration

purposes, the loading takes on the following analytic form:

$$\frac{d\bar{v}}{dx} = 6\Delta\bar{v}\, x(1-x) \tag{4-1}$$

where $\Delta\bar{v}(x) = \bar{v}_{\mathrm{TE}} - \bar{v}_{\mathrm{LE}}$ is the overall change in mass-averaged tangential velocity. The blades axial chord is used as reference length and the subscripts LE / TE refer to the blades leading/trailing edge.

It is worth noting that, at the blades leading and trailing edges (whether sharp or round), all flow variables have to be continuous so that $p = p^+ = p^-$ hence the loading $d\bar{v}/dx$ has to vanish at both LE and TE. Therefore, the Kutta condition, implying flow continuity at a sharp TE, is directly and exactly satisfied by setting $d\bar{v}/dx = 0$. Moreover, the incidence angle is simulated by a loading distribution which has a sharp rise near the LE and the deviation angle is part of the solution. This effect will be reflected in the choice of mass-averaged swirl distribution.

It was found that the computing time required for a design calculation varies between 0.5 and 2 times that of an analysis calculation.

4.1 Parabolic Cascade

To validate the design method, a parabolic cascade is first analyzed by running the FVM code in design mode, the prescribed loading and thickness distributions assume a parabolic profile. The loading distribution is given in equation (4-1) while the thickness distribution

is given by the following form:

$$T(x) = 6T_{\max}x(1-x) \tag{4-2}$$

This loading distribution is symmetric around mid-chord and this prescribed thickness distribution implies sharp LE and TE. The maximum thickness $T_{\max}$ is 4.1%, the flow inlet and exit angles are 9.3° resulting in a $\Delta\bar{v} = 0.174$, the spacing-to-chord ratio is 0.5 and the ratio of exit static to inlet total pressure is 0.84. The resulting blade shape is then analyzed by running the same code but in analysis mode. If this design method is valid, then the results of the two runs should be identical (to within a tolerance), in particular, the analysis run should result in the same prescribed loading.

This validation case was implemented using both a sheared H-mesh and a Delauney mesh. The sheared H-mesh is composed of 40 nodes in the y-direction (the pitch-wise direction) and 40/170/40 in the x-direction (stream-wise direction), and the Delauney mesh is composed of 7690 nodes and 14978 triangles. The iso-Mach lines for both design and analysis calculations are compared in Figure 4-1. The pressure distribution along the upper and lower surfaces of the blade is shown in Figure 4-2 and the mass-averaged tangential velocity computed from analysis is compared with the one prescribed in the design mode in Figure 4-3. These results confirm the agreement between the two solutions, hence validating this design method.

4.2 Subsonic Compressor Cascade

To validate the design method, the flow around a subsonic compressor cascade with a round LE and a sharp TE is first simulated by running the FVM code in design mode, with a loading that varies according to the following form:

$$\frac{d\bar{v}}{dx} = \Delta\bar{v}\left[\frac{a^2+\pi^2}{\pi(1+e^{-a})}\right] e^{-ax}\sin\pi x \tag{4-3}$$

where $a = \pi/\tan\pi x_0$ and x_0 is the location of maximum loading. The thickness distribution assumes the following profile:

$$T(x) = \frac{3\sqrt{3}}{2} T_{\max}\sqrt{x}(1-x) \tag{4-4}$$

which implies a round LE and a sharp TE. The maximum thickness $T_{\max} = 12\%$ and occurs at mid chord, the flow inlet angle is 25.6°, and the overall turning is $\Delta\bar{v} = 0.345$, the spacing-to-chord ratio is one and the exit static to inlet total pressure is 0.9. The blade shape resulting from the design calculation is then analyzed by running the same code but in analysis mode.

The convergence history of the analysis and design runs, given in Figure 4-4, shows that both runs converge to machine accuracy and the convergence rate of the analysis run is about 1.4 times of the design run for this particular case. The mesh used in this calculation is given in Figure 4-5 with a close-up view of the leading edge area.

The pressure distribution along the upper and lower surfaces of the blade and the mass-averaged tangential velocity computed from analysis and design are compared in

Figures 4-6 and 4-7. These figures confirm the agreement between the two solutions hence validating the present design approach.

To test the robustness of the inverse design code, the initial guess for the camber line is taken to be zero, i.e. a symmetric airfoil and the design iterations are started from that symmetric airfoil and are run to convergence. Figure 4-8 shows the evolution of the blade profile from a symmetric one to the final one which has a maximum camber of 15% chord.

4.3 Turbine Inlet Guide Vane

To validate the design method for a fat cascade with round LE & TE, a subsonic turbine inlet guide vane with analytical thickness distribution:

$$T(x) = 2T_{\max}\sqrt{x(1-x)} \tag{4-5}$$

is first analyzed by running the FVM code in design mode, the prescribed loading and thickness distributions assume a parabolic profile. The maximum thickness is 25%, the flow inlet and exit angles are 0° and 50°, respectively, the spacing-to-chord ratio is 1 and the exit static to inlet total pressure is 0.9. The resulting blade shape is then analyzed by running the same code but in analysis mode.

The pressure distribution along the upper and lower surfaces of the blade computed from analysis and design is shown in Figure 4-9 and the mass-averaged tangential velocity computed from analysis is compared with the prescribed one in design in Figure 4-10.

These figures confirm once again the agreement between the two solutions for this fat cascade with round LE and TE.

4.4 Parametric Study of Loading Distribution

The effect of the loading distribution on the blade shape and the incidence angle was carried out for the parabolic cascade given in § 4.1.

4.4.1 Effect of Loading on the Blade Shape

Three different loading distributions were applied to the parabolic cascade, where they assume the variation form according to equation (4-3).

These three loading distributions differ in the location of a which corresponds to 20%, 50% and 80% chord, respectively. Figure 4-11 shows the resulting blade profile when the above three loading distributions is applied. It should be noted that all loadings accomplish the same overall flow turning, i.e. the same global performance.

The effect of loading on the blade shape can be physically interpreted as follows. The loading is proportional to $d\bar{v}/dx$, hence $\bar{v}(x)$ for a front loaded airfoil would vary more rapidly in the front part of the airfoil. Since the flow is tangent to the blades, then df/dx is proportional to v/u, hence df/dx (and f) will also vary more rapidly in the LE area,

provided that the x-component of velocity u is of order 1. This explains the resulting blade shapes.

4.4.2 Effect of Loading on the Incidence Angle

To show how the incidence angle is affected by the loading distribution, two different loading profiles, which have the same overall flow turning $\bar{v}(x)$ and the same location for maximum loading but have different loading shapes, have been prescribed. The two loading distributions vary according to equation (4-3) and the following equation:

$$\begin{aligned} \frac{d\bar{v}}{dx} &= \frac{\pi}{2}\Delta\bar{v}\,\sin\frac{\pi x}{2x_0} && 0 < x < x_0 \\ \frac{d\bar{v}}{dx} &= \frac{\pi}{2}\Delta\bar{v}\,\cos\frac{\pi(x-x_0)}{2(1-x_0)} && x \geq x_0 \end{aligned} \tag{4-6}$$

where x_0 is the location of maximum loading.

These loadings are given in Figure 4-12 where one can see clearly that the location of maximum loading is the same but the value of maximum loading is different, this is expected since both loadings accomplish the same amount of turning, i.e. the area under these two curves has to be the same. The resulting blades are shown in Figure 4-13. The incidence angle, which is defined as the difference between the inflow angle and the slope of the camber line at the blades LE, increases as the value of the maximum loading increases.

4.5 Transonic Impulse Turbine Cascade

To present the usefulness of the inverse design method in removing shocks, an impulse turbine cascade is first analyzed. The inlet flow angle is 40.63°, the overall turning is $\Delta\bar{v} = 0.751$, and the exit static pressure is 0.84. The spacing-to-chord ratio is 0.526 and both camber line and thickness distributions assume a parabolic profile with a maximum camber of 21.45% and a maximum thickness of 21.45% chord. Figure 4-14A shows that a shock occurs around 60% chord. This blade is then redesigned to eliminate that shock keeping the same overall flow turning, the same thickness distribution, and the same pressure rise (exit static to inlet total pressure ratio). The prescribed loading distribution is chosen to be a smooth parabolic one. The resulting transonic flow is shock-free, as can be seen in Figure 4-14B. The static pressure along the blade suction and pressure sides and the blade profile for both original and modified design are compared in Figure 4-15. A comparison of the blade profiles, given in Figure 4-16, shows that, to eliminate the shock, the redesigned blade has a reversed curvature along both suction and pressure sides to allow the flow to compress reversibly. This reversed curvature was also observed by Dang [32] and Cumpsty [36] to remove the passage shock when designing transonic compressor blades.

4.6 ONERA Compressor Cascade

The third test case is that of a highly loaded transonic compressor cascade, tested at ONERA [13]. This compressor cascade has been redesigned using the present method to remove the passage shock. The inlet flow angle is 39°, the exit static pressure is 0.77 and the blades thickness distribution is given in [13]. This cascade was first analyzed and the Mach number field, given in Figure 4-17A, shows the presence of a shock on the suction side where the maximum Mach number is around $M = 1.65$. A parametric study was carried out to see the effect of the prescribed swirl distribution on the blade shape and on the flow field particularly on the position and strength of the passage shock, shown in Figure 4-17A. To compare the original and the redesigned blades, the corrected mass flow rate $\dot{m}\sqrt{T_o}/p_o$ as well as the overall flow turning $\Delta\bar{v}$ were fixed. That parametric study showed that a parabolic loading distribution did remove the shock, as can be seen in Figure 4-17B, and the flow in the redesigned cascade is transonic with a maximum Mach number of 1.14. The static pressure along the blade suction and pressure sides and the blade loading for both original and modified design are compared in Figure 4-18. It is interesting to note the drastic change in camber line between the original and the redesigned cases which is due to the fact that the original blade is front loaded whereas the redesigned blade has a loading that is symmetric around mid-chord. This implies that, from 0 to 50% chord, $\bar{v}$ in the redesigned case (and hence df/dx) is larger than that of the analysis case.

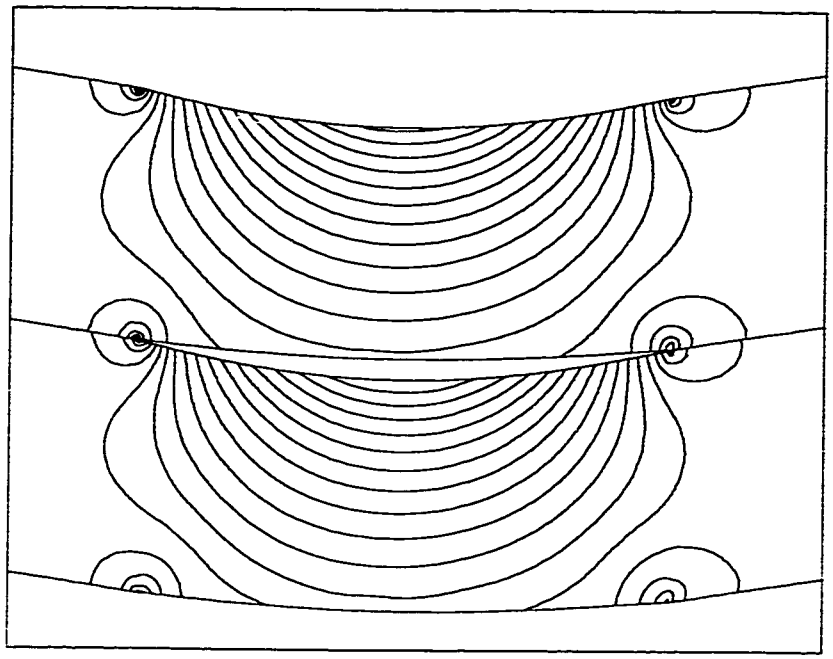

Figure 4-1: Mach isolines, analysis (top) and design (bottom).

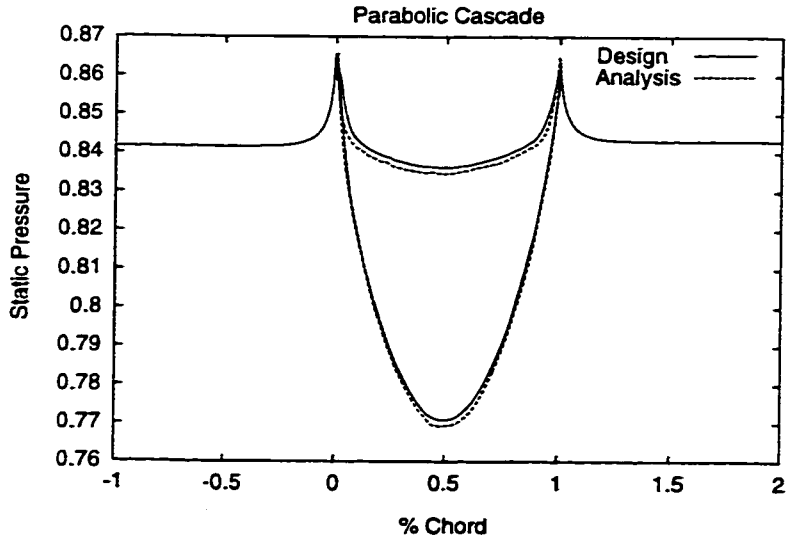

Figure 4-2: Static pressure along the pressure and suction sides of the blade.

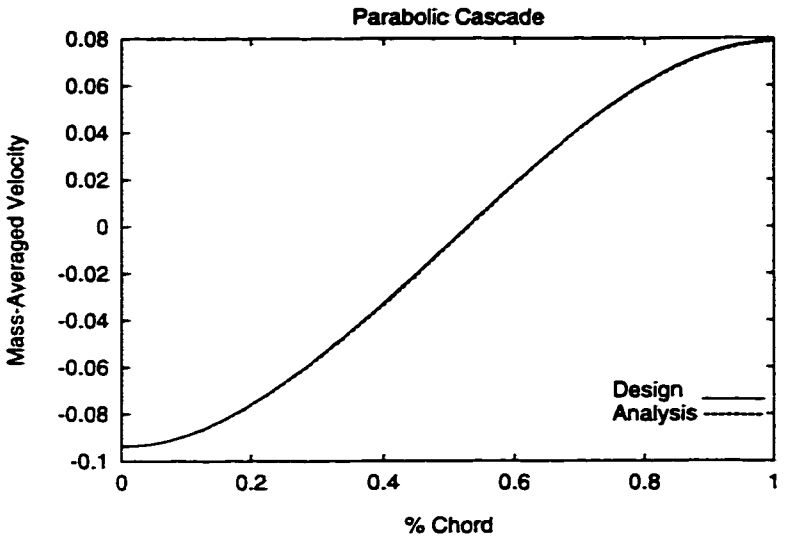

Figure 4-3: Mass-averaged tangential velocity distribution in the bladed region.

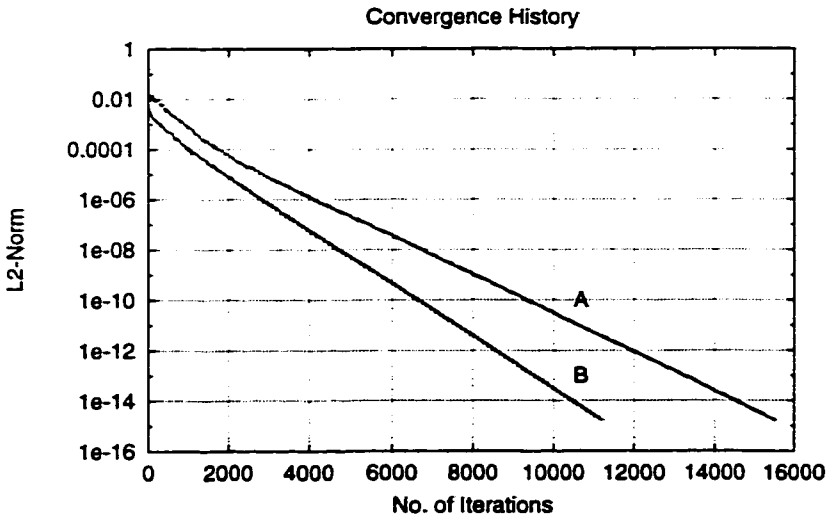

Figure 4-4: Convergence histories for analysis (A) and design (B) of a compressor cascade.

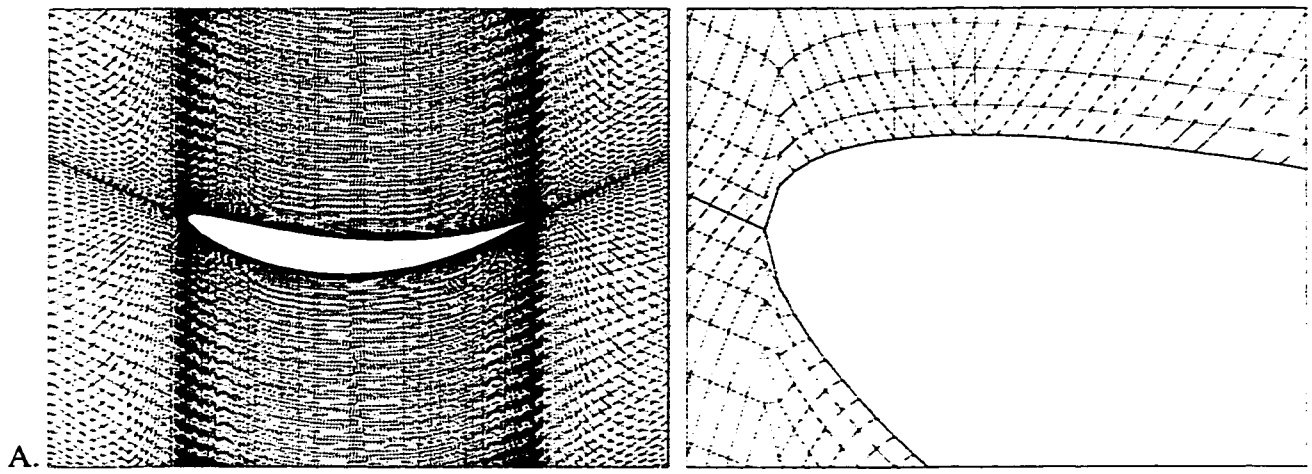

Figure 4-5: Mesh for compressor cascade validation.

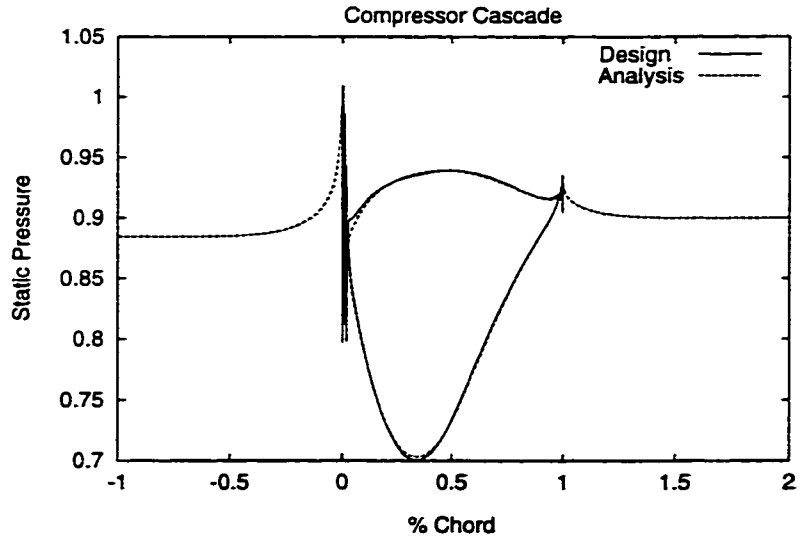

Figure 4-6: Static pressure along the blade pressure and suction sides.

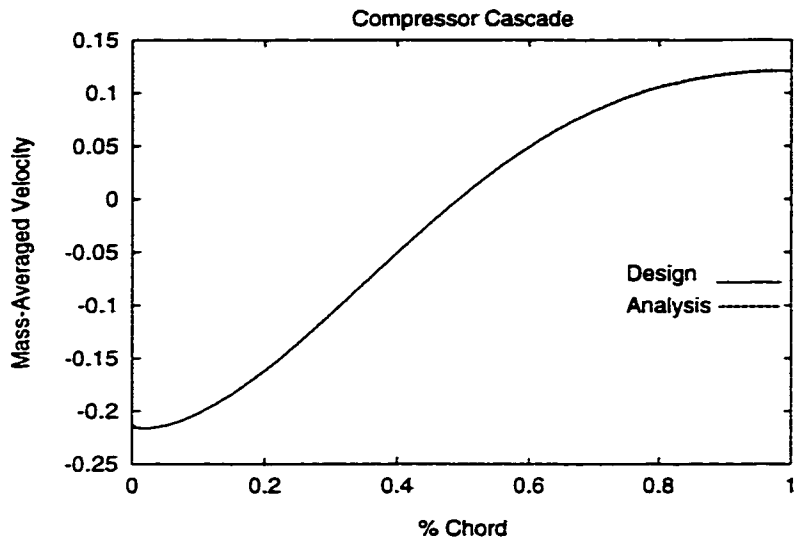

Figure 4-7: Mass-averaged tangential velocity distribution in the bladed region.

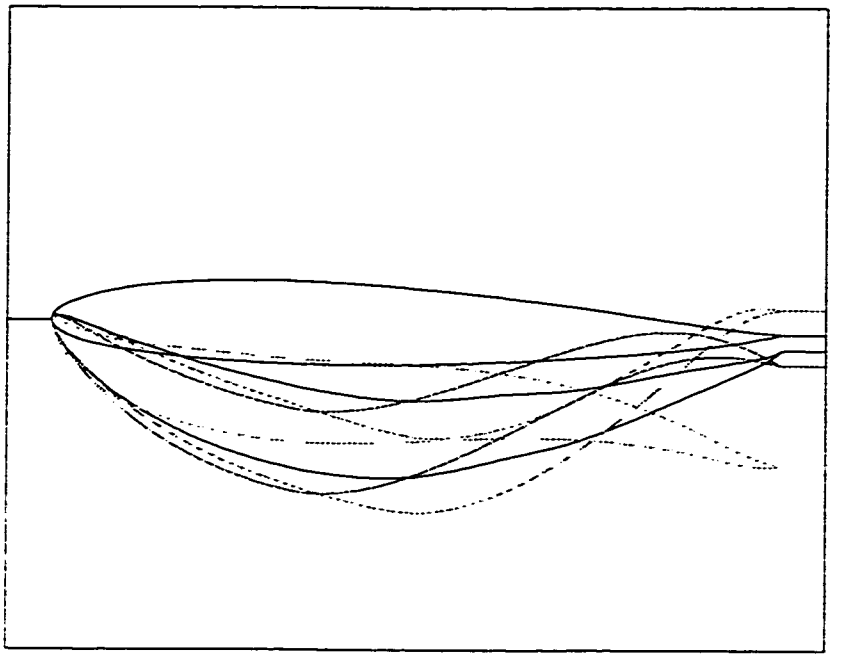

Figure 4-8: The evolution of the compressor blade profile from a symmetric one (solid line) to the final one which has a maximum camber of 15% chord (solid line).

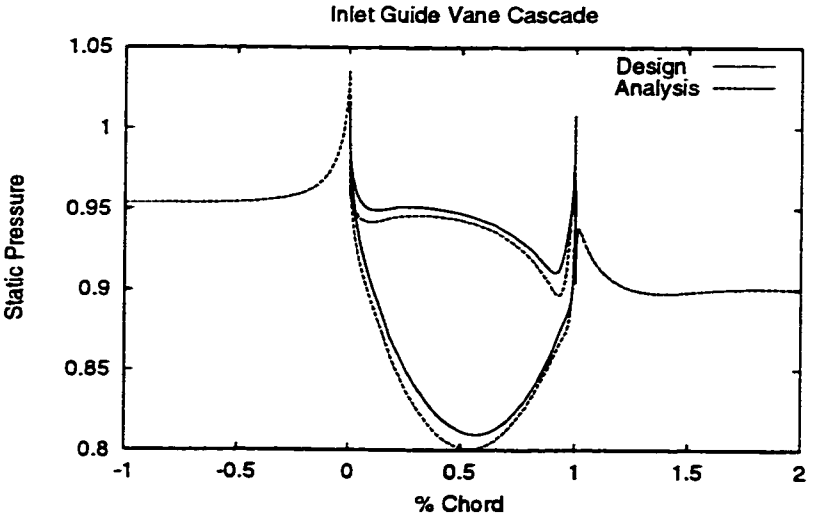

Figure 4-9: Static pressure along the pressure and suction sides of the blade.

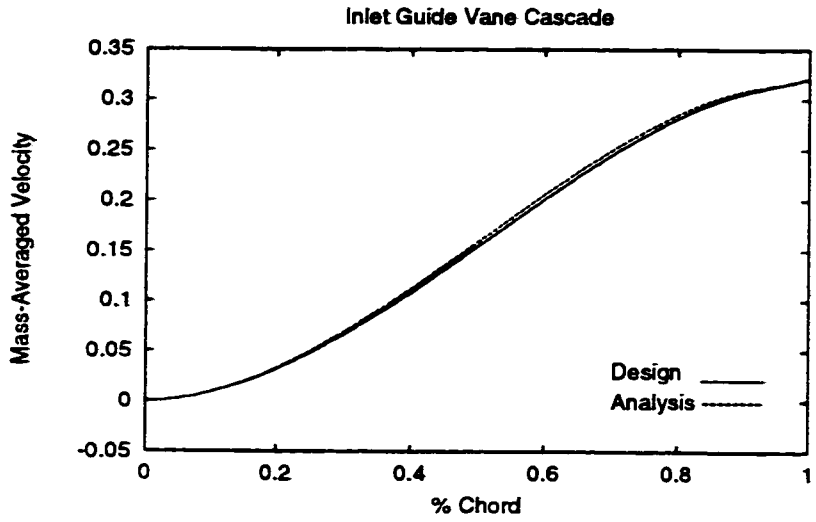

Figure 4-10: Mass-averaged tangential velocity distribution in the bladed region.

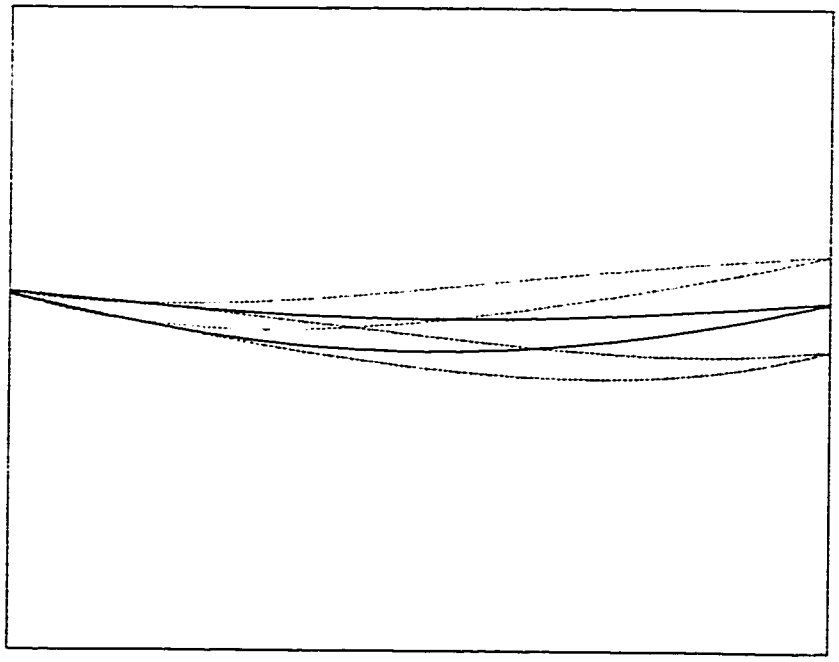

Figure 4-11: Effect of loading distribution on the blade profile.

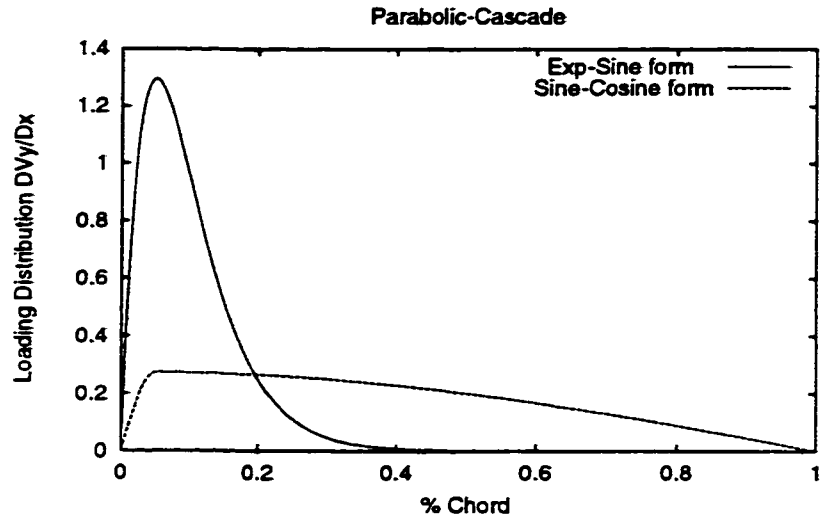

Figure 4-12: Loading distributions.

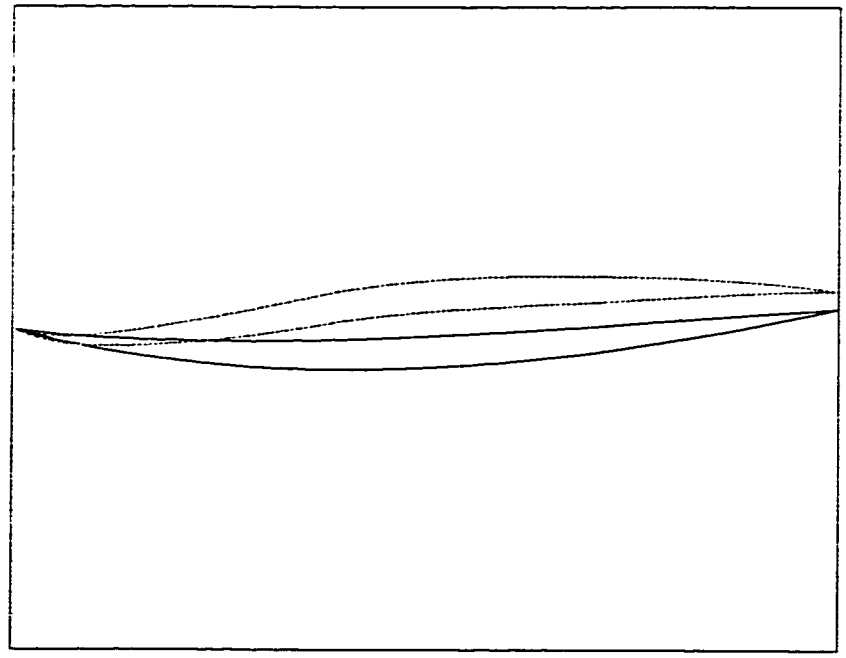

Figure 4-13: Effect of loading (solid line: sine-cosine form and dashed line: exponential-sine form) on incidence angle.

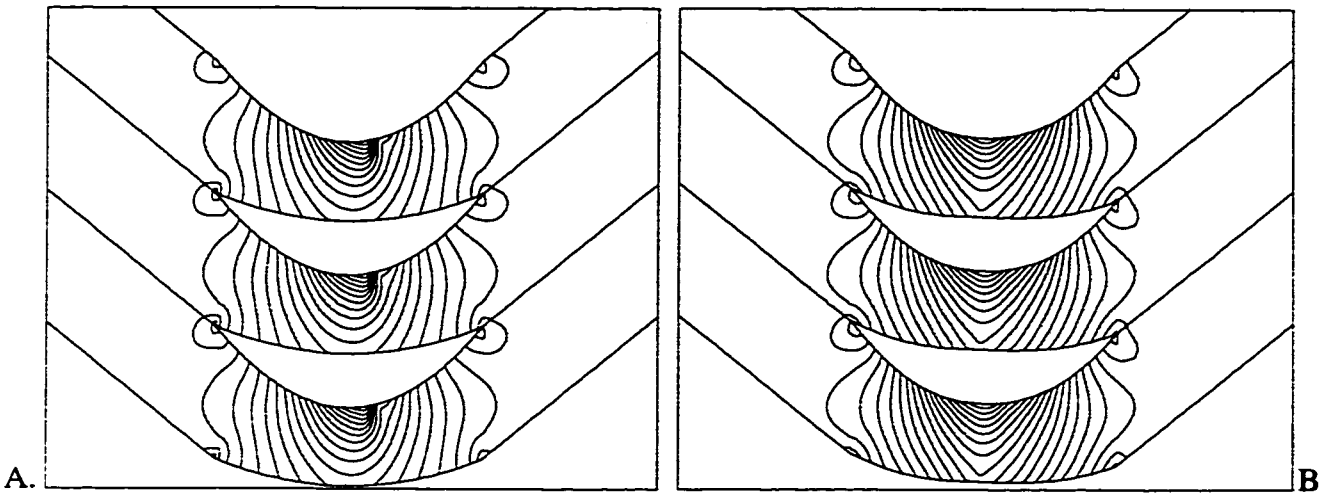

Figure 4-14: Mach isolines: The original (A) and the improved design (B) of an Impulse turbine cascade.

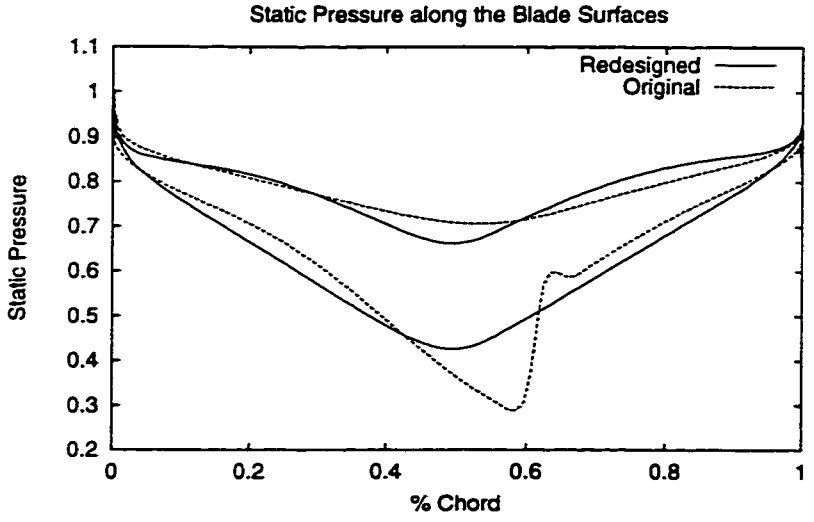

Figure 4-15: Static pressure along the blade surfaces for the original and the modified blades.

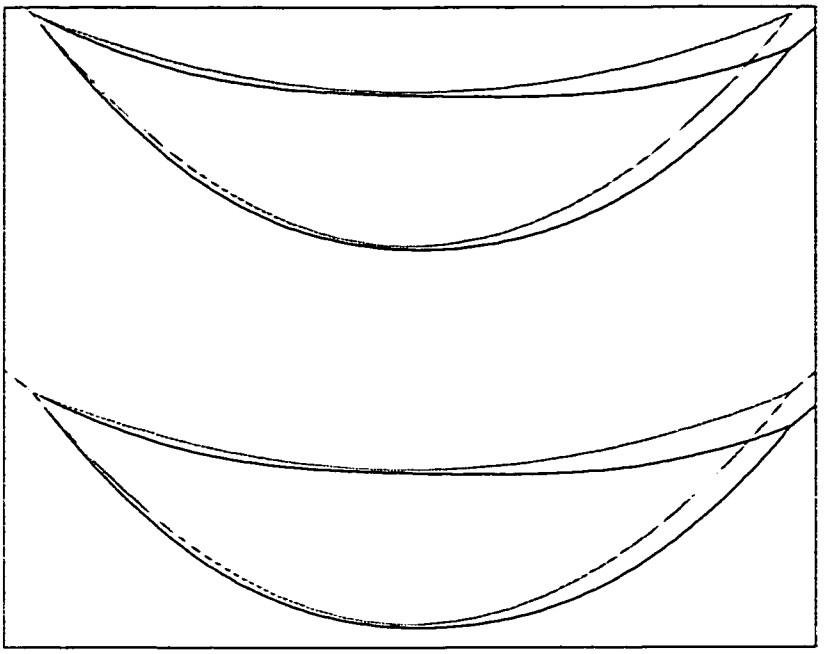

Figure 4-16: Original and modified (solid lines) blade profiles.

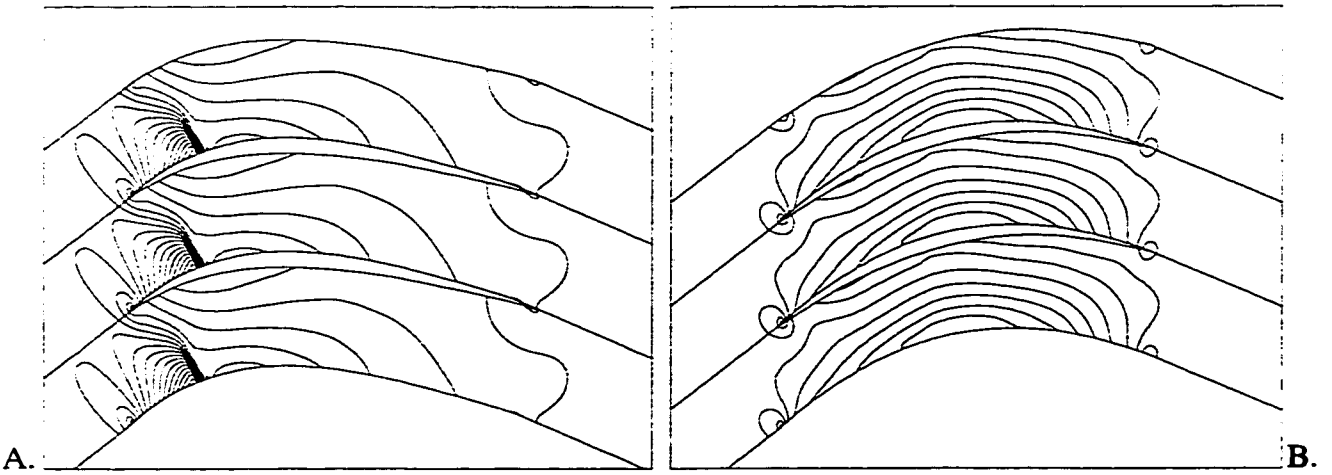

Figure 4-17: Mach isolines: The original (A) and redesigned (B) blades of the ONERA cascade.

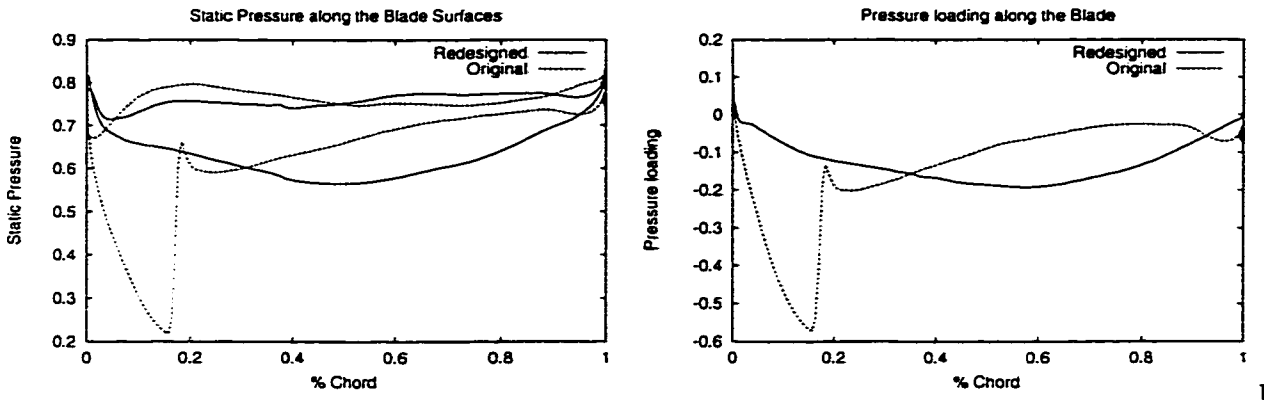

A. B.

Figure 4-18: Static pressure along the blade surfaces (A) and the corresponding pressure loading (B) for the original and redesigned blades.

Chapter 5

Conclusion

An aerodynamic inverse design method for transonic turbomachinery cascades has been presented and implemented using the finite volume method. The mass-averaged tangential velocity and the thickness distribution are the prescribed design variables. This design method is implemented in a cell-vertex finite volume scheme where the two-dimensional Euler equations are solved on an unstructured triangular mesh. The steady state solution is reached by pseudo-time marching the Euler equations using an explicit five-stage Runge-Kutta scheme. Local time stepping and implicit residual smoothing were used for convergence acceleration. The non-linear blend of second and fourth order artificial viscosity was found to be successful in capturing shocks and eliminating pressure-velocity decoupling with minimal numerical diffusion. The method of characteristics, used to impose inflow and outflow boundary conditions, allowed for placing the boundary relatively closer to the

body. The only difference between the analysis and design modes of computation lies in the boundary conditions along the blade surfaces. In the analysis mode, the conventional flow tangency condition is implemented whereas, in the design mode, the flow tangency condition results in the imposition of the y-component of velocity and the blades camber line.

The design method has been validated for different compressor and turbine cascade configurations. It was shown that, for the cases that were tested in this work, the inverse design method is relatively insensitive to the initial guess of the camber line profile. A parametric study on the effect of the different loading distributions on the blade profile and on the incidence angle, demonstrated that the blade shape is rather sensitive to the loading distribution. The usefulness of this inverse design method in designing shock-free transonic cascades has also been demonstrated.

5.1 Future Work

There are several possible extensions to the present inverse design method. To list a few:

1. The present design method can be readly extended to simulate viscous flows. The viscous effects can be accounted for using a body force representation, following the work of Denton [11].

2. It can be extended to three-dimensional flow in annular blade rows as follows. The

prescribed quantities will be the swirl schedule $r\bar{v}_\theta(r,z)$, the blade tangential thickness distribution $T(x)$ and the stacking line. The Euler equations, written in cylindrical coordinates, are then solved with a design boundary condition similar to the one implemented in this work, to give the 3D blade camber surface. This design method can be easily incorporated into current industrial design systems as follows. The current practice is to obtain a radial distribution of flow variables by running a through-flow analysis. Blade sections at different radii and a stacking condition are then assumed and the flow is then simulated. This design method can be introduced in to the design system by taking the overall turning that is produced by the through-flow analysis and use it as input to the design method which then provides the blade shape.

3. Another interesting extension would be to couple this design method with an optimization technique to allow for the addition of some constraints. A typical example occurs in turbine cascades where the plan-form area is limited near the hub section, therefore a maximum camber should be prescribed.

Bibliography

[1] Gostelow, J.-P. (1995) 'Some unresolved physical problems in two-dimensional flows around blading,' in *Turbomachinery Fluid Dynamics and Heat Transfer Conference*, University Park, PA.

[2] Meauze, G. (1989) 'Blading Design for Axial Turbomachines, Overview on Blading Design Methods,' AGARD–LS–167, Propulsion and Energetics Panel.

[3] Zanetti, L., Larocca, F., and Marsilio, R. (1989) 'Computational Methods for Aerodynamic Design (Inverse) and Optimization, Numerical Method for Designing 3D Turbomachinery Blade Rows,' AGARD–CP–463, Fluid Dynamics Panel.

[4] Moore, J. (1976) 'Eckardt's impeller- a ghost from ages past,' Tech. Rep. Turbo TR–83, Cambridge University, London, UK.

[5] Baines, N., Wallace, F., and Whitfield, A. (1978) 'Computer aided design of mixed flow turbines for turbochargers,' *ASME* Paper no. 78–GT–191.

[6] Jameson, A., Baker, T., and Weatherill, N. (1986) 'Calculation of inviscid transonic flow over a complete aircraft,' *AIAA* Paper no. 86–0103.

[7] Arnone, A. and Stecco, S. (1989) 'Inviscid cascade flow calculations using a multigrid method,' *ASME* Paper no. 89–GT–22.

[8] Adamczyk, J., Celestina, M., Beach, T., and Barnett, M. (1989) 'Simulation of 3D viscous flow within a multistage turbine,' *ASME Journal of Turbomachinery*, 112, 370–376.

[9] Siden, G., Dawes, W., and Albraten, P. (1990) 'Numerical simulation of the two-dimensional viscous compressible flow in blade cascades using a solution-adaptive unstructured mesh,' *ASME Journal of Turbomachinery*, 112, 311–319.

[10] Dawes, W. (1992) 'Toward improved through-flow capability: The use of three-dimensional viscous flow solvers in a multistage environment,' *ASME Journal of Turbomachinery*, 114, 8–17.

[11] Denton, J. (1992) 'The calculation of three-dimensional viscous flow through multistage turbomachines,' *ASME Journal of Turbomachinery*, 114, 18–26.

[12] Liu, F. and Jameson, A. (1993) 'Cascade flow calculations by a multigrid Euler method,' *AIAA Journal of Propulsion and Power*, **9(1)**, 90–97.

[13] Fottner, L. (1990) 'Test Cases for Computation of Internal Flows in Aero Engine Components,' AGARD–AR–275, Propulsion and Energetics Panel.

[14] Irmisch, S. (1994) 'Adaptive finite-volume solution of the two-dimensional Euler equations on unstructured meshes,' *ASME* Paper no. 94–GT–87.

[15] Mavriplis, D. (1990) 'Accurate multigrid solution of the Euler equations on unstructured and adaptive meshes,' *AIAA Journal*, **26(2)**, 213–221.

[16] Mavriplis, D. (1987) *Solution of the Two-Dimensional Euler Equations on Unstructured Triangular Meshes*, Ph.D. thesis, Princeton University.

[17] Jameson, A., Schmidt, W., and Turkel, E. (1981) 'Numerical solution of the Euler equations by finite volume methods using Runge-Kutta time-stepping schemes,' *AIAA* Paper no. 81–1259.

[18] Holmes, D. and Connell, S. (1989) 'Solution of the 2D Navier-Stokes equations on unstructured adaptive meshes,' *AIAA* Paper no. 89–1932.

[19] Giles, M. (1986) 'UNSFLO: A numerical method for the unsteady inviscid flow in turbomachinery,' Tech. Rep. CFDL–TR–86–6, MIT.

[20] Giles, M. (1990) 'Nonreflecting boundary conditions for Euler equation calculations,' *AIAA Journal*, **28(12)**, 2050–2058.

[21] Lighthill, M. (1945) 'A new method of two-dimensional aerodynamic design,' in *Aeronautical Research Council RxM 2104.*

[22] Giles, M. and Drela, M. (1987) 'Two-dimensional transonic aerodynamic design method,' *AIAA Journal*, **25(9)**, 1199–1205.

[23] Zhengming, W. (1985) 'Inverse design calculations for transonic cascades,' *ASME* Paper no. 85–GT–6.

[24] Leonard, O. and Van Den Braembussche, R. (1992) 'Two-dimensional transonic aerodynamic design method,' *ASME Journal of Turbomachinery*, **114(3)**, 553–560.

[25] Novak, R. and Haymann-Haber (1983) 'A mixed-flow cascade passage design procedure based on a power series expansion,' *Journal of Engineering for Gas Turbines and Power*, 105, 231–242.

[26] Zannetti, L. and Pandolfi, M. (1984) 'Inverse design technique for cascades,' NASA CR 3836.

[27] Tan, C., Hawthorne, W., McCune, J., and Wang, W. (1984) 'Theory of blade design for large deflections: Part II- annular cascades,' *Journal of Engineering for Gas Turbines and Power*, **106(2)**, 354–365.

[28] Borges, J. (1990) 'A three-dimensional inverse method for turbomachinery: Part I-theory,' *ASME Journal of Turbomachinery*, **112(3)**, 346–354.

[29] Ghaly, W. (1990) 'A design method for turbomachinery blading in three-dimensional flow,' *International Journal for Numerical Methods in Fluids*, **10(2)**, 179–198.

[30] Dang, T. (1993) 'A fully three-dimensional inverse method for turbomachinery blading in transonic flow,' *ASME Journal of Turbomachinery*, **115(2)**, 354–361.

[31] Dang, T. and Jiang, J. (1994) 'Design method for turbomachine blades with finite thickness by the circulation method,' *ASME* Paper no. 94–GT–368.

[32] Dang, T. (1995) 'Inverse method for turbomachine blades using shock-capturing techniques,' *AIAA* Paper no. 95–2465.

[33] Dang, T., Nerurkar, A., and Reddy, D. (1997) 'Design modification of rotor 67 by 3D inverse method – inviscid-flow limit,' *ASME* Paper no. 97–GT–484.

[34] Lindquist, D. (1988) *A Comparison of Numerical Schemes on Triangular and Quadrilateral Meshes*, Master's thesis, MIT.

[35] Vinokur, M. (1983) 'On one-dimensional stretching functions for finite-difference calculations,' *Journal of Computational Physics*, 50, 215–234.

[36] Cumpsty, N. (1989) *Compressor Aerodynamics*, Longman Scientific & Technical.

[37] Dompierre, J., Vallet, M. G., Fortin, M., and Habashi, W. (1995) 'Edge-based mesh adaptation for CFD,' in *Conference on Numerical Methods for the Euler and Navier-Stokes Equations*, pp. 265–299, Montreal, Canada.

[38] Fortin, M., Vallet, M. G., Dompierre, J., Bourgault, Y., and Habashi, W. (1996) 'Anisotropic mesh adaption: Theory, validation and 2-D applications,' in *Third EC-COMAS Computational Fluid Dynamics Conference*, Paris, France.

[39] Vallet, M.-G., Dompierre, J., Bourgault, Y., Fortin, M., and Habashi, W. (1996) 'Coupling flow solvers and grid through an edge-based adaptive grid method,' in *ASME Fluids Engineering Conference*, San Diego, CA.

[40] Anderson, J. (1990) *Modern Compressible Flow*, McGraw-Hill Publishing Company.

[41] Rizzi, A. and Viviand, H. (1981) 'Numerical methods for the computation of inviscid transonic flows with shock waves,' in *Notes on Numerical Fluid Mechanics, Vol. 26.*

[42] Denton, J. (1983) 'An improved time marching method for turbomachinery flow calculation,' *Journal of Engineering for Gas Turbines and Power*, 105, 514–521.

Appendix A

Validation of the Finite Volume Solver

In this appendix, the FVM solver described in chapter 3 is validated against a number of internal subsonic, transonic and supersonic test cases. Also the solver is applied to two theoretical cascade and one practical cascade, namely the Hobson shock-free impulse cascade, Denton's supersonic wedge cascade and the ONERA transonic compressor cascade given in Fottner [13]. A mesh adaptation library LIBOM, described below, has been used to optimize the solution obtained from the finite volume solver.

A.1 Mesh Adaptation

A mesh adaptation library LIBOM, described in Dompierre *et al.* [37] has been used in the present work to show the capability of the finite volume solver with mesh adaptation. This library is summarized here-after.

In any adaptive meshing procedure, there are two basic elements: a) an error estimator to quantify the mesh quality and give directives for mesh improvement so as to minimize and equi-distribute the estimated errors, and b) a mesher that would implement the directives given by the error estimator and create the adapted mesh.

The ideal error estimator is the discretization error $||U_{\text{exact}} - U_{\text{numerical}}||$, however, as this error is inaccessible, the interpolation error $||U_{\text{exact}} - U_{\text{interpolated}}||$, which bounds the actual error, will be used as error estimator. When the discretization is based on a piecewise constant function, e.g. a cell centered FVM, the interpolation error is obtained from the solution gradients. However, when piecewise linear functions are used, e.g. cell-vertex FVM, the error based on the gradient becomes less effective, and adaptation must be based on second derivatives, i.e. the mesh will be refined in regions where the solution curvature is large. Therefore, the error estimator is based on second derivatives, that is the Hessian matrix of the numerical solution $U_{\text{numerical}}$. The second derivatives of a piecewise linear function are then evaluated in a weak sense using integration by parts. The eigenvalues of this Hessian matrix correspond to the error scales and the eigenvectors give the principal directions of these errors. Hence, this error estimator provides directional error estimates, more details can be found in Dompierre *et al.* [37].

The next task is to construct a mesh that will equi-distribute the calculated error. To keep the directional character of the error estimator, the error over the edges is evaluated and is used to construct an anisotropic mesh with triangles and/or cells stretched in the

direction of maximum error. Starting from the current mesh, this new mesh is constructed using four simple local operations: mesh refinement, mesh coarsening, node relocation and node reconnection. Each of these operations has the effect of equi-distributing the error estimate over the edges. Convergence of this mesh adaptation process is demonstrated in Fortin *et al.* [38].

The mesh adaptation library LIBOM is solver-independent. Given a starting mesh, the solver is first called for a certain number of iterations. The solution thus obtained is passed on to the mesh adaptor which adapts it as described above, the control is then passed on to the solver and so on. This process is repeated until convergence of both mesher and solver as shown in Vallet *et al.* [39].

In the present work, the solution was started on a uniform Delaunay mesh and the residual was reduced by four orders of magnitude, the solver-mesher loop was then started and the solver was allowed to converge one order of magnitude before remeshing. Typically 5 to 10 mesher-solver iterations were needed to obtain a converged solution. The time taken by the mesher is negligible compared to that taken by the solver.

A.2 Supersonic Compression Corner

The first test case is that of a supersonic compression corner with an inlet Mach number of 3.0 and a wedge angle of 15°. Figure A.1 shows the initial Delaunay mesh composed of

8583 nodes and the iso-Mach lines computed on that mesh, whereas Figure A.2 shows the adapted mesh with 1188 nodes and the corresponding solution.

A close view of the shock region on the initial and adapted meshes, given in Figure A.3, shows that the shock is captured on two to three triangles (i.e. one to two cells). However, on the adapted mesh, the elements in the shock region have an aspect ratio of about 50, i.e. the shock is 50 times thinner. The computed shock angle is 17.4° compared to the exact value of 17.5° [40].

A.3 A 15° Wedge in a Channel

The supersonic ($M = 2.0$) and subsonic ($M = 0.5$) flows over a 15° wedge in a channel are considered. The results obtained for supersonic test case using Delaunay triangulation and those obtained using directional adaptation are compared in Figure A.4. The supersonic flow features, namely the oblique shock at the beginning of the ramp, the expansion fan at the end of the ramp and the shock reflection are well captured. The convergence history for the initial mesh is shown in Figure A.5. The convergence rate is increased by a factor of three using implicit residual smoothing. The convergence rate is unaffected by mesh adaptation.

Figure A.6 presents iso-Mach lines for the subsonic case, where $M = 0.5$ at the outflow boundary. The smoothness of the Mach isolines reflects the high-accuracy of the AV

scheme. As the ramp starts near the inflow section, it was not possible to obtain a converged solution when a zero order space extrapolation was used as boundary condition at inflow, therefore the current boundary condition implementation has proved to be relatively more robust.

A.4 GAMM-Bump with 4.2 % and 4 %

The third test case is that of the transonic and supersonic flows in a channel with a 4.2 % and 4.0 % circular arc bumps, respectively. The transonic case is taken from the GAMM-test cases [41]. The exit Mach number for the transonic case is 0.85 and inlet Mach number for the supersonic one is 1.4.

In the case of the transonic bump, there is a transonic bubble followed by a normal shock near the bump trailing edge. Figure A.7 shows the original and the adapted meshes. When the solver has partially converged on the original mesh, the mesh adaptation library is called and, after ten solver-mesher cycles, the grid is reduced from 7863 to 5119 nodes. It should be noted that the shock is captured on two to three triangles (i.e. one to two cells). On the adapted mesh, the elements in the shock region have an aspect ratio of about 100, i.e. the shock is 100 times thinner as can be seen in Figure A.8. The numerical results for C_p along the lower wall agree rather well with the experimental values, as shown in Figure A.9.

For the supersonic bump, compression shocks form at the bump leading and trailing edges, reflect from the wall and interact. Figure A.10 shows the shock-shock and shock-wall interactions for the original and the adapted meshes. The shocks are captured on the initial mesh and are much thinner on the adapted mesh.

A.5 Blunt body

The supersonic flow ($M = 3.0$) around a circular blunt body is considered. The adapted mesh and the Mach contours are shown in Figure A.11. The detached bow shock is accurately captured. The adapted mesh indicates that the solution second derivative is high only in the shock region and is more or less uniform downstream of the shock where the flow decelerates and turns around the blunt body. It should be mentioned that, for this particular case, the solution obtained on the initial (unadapted) mesh did capture the shock however, it did not correctly predict the shock strength.

A.6 Hobson Turbine Cascade

The second test case is the Hobson shock-free impulse turbine cascade [13]. At inlet, the flow angle is 46.123° and Mach number is 0.575. The total enthalpy, entropy and flow angle are taken to be uniform at inlet and the static pressure at exit is chosen such as to give the specified Mach number there. Since the flow is symmetric about mid-chord, the inlet

and exit Mach numbers are equal. The Mach contours, given in Figure A.12, show that the numerical solution is indeed symmetric and shock free. The numerical and analytical Mach number distributions along the suction and pressure surfaces, plotted in Figure A.13, are in good agreement. The original and adapted meshes, composed of 849 and 697 nodes respectively, are given in Figure A.14. Note that the initial mesh was manually optimized using stretching factors in the mesh generator. Note also that, as there are no large gradients in anyone direction, the adapted mesh is rather isotropic and is also symmetric as the flow is symmetric around mid-chord.

A.7 Supersonic Wedge Cascade

The next test case is Denton's supersonic wedge cascade [13], for which an exact solution exists. This wedge is designed such that the shock ensuing from the leading edge, after reflection on the pressure surface, is exactly cancelled at the first corner on the suction surface. Denton [42] and Liu and Jameson [12] analyzed a similar configuration and their results suggest that a mesh adaptation would be needed to properly resolve the flow features for that case. The original and the directionally adapted meshes are shown in Figure A.15 and the corresponding iso-Mach lines are compared in Figure A.16. The adapted solution is obtained after four solver-mesher cycles, where the grid has been increased from 1534 to 3371 nodes with a high concentration in the shocks and expansion fan areas. The

flow features are evident by examining the adapted mesh, and the corresponding iso-Mach contours. The adapted solution has uniform flow regions except in the shocks and the expansion fans. The numerical and analytical Mach number distributions along the pressure and suction sides of the wedge, given in Figure A.17, show that the numerical and analytical Mach number levels are in good agreement, the shocks are captured rather well with about 2 to 3 % overshoot and the cancellation of the shock off of the first corner is also evident.

A.8 ONERA Compressor Cascade

The last test case is that of a transonic flow through a highly loaded double circular arcs compressor cascade, tested at ONERA and compiled in Fottner [13]. The inlet Mach number and the flow angle are 0.85 and 50°, respectively. The original and the adapted meshes are shown in Figure A.18 and the corresponding iso-Mach contours are shown in Figure A.19. The grid is increased from 1473 to 1900 nodes with a significant concentration in the shock and the trailing edge areas. On the original and the adapted meshes, the shock is captured, however, on the adapted mesh, the shock is much thinner which demonstrates the ability of both solver and mesh adaptor in shock capturing.

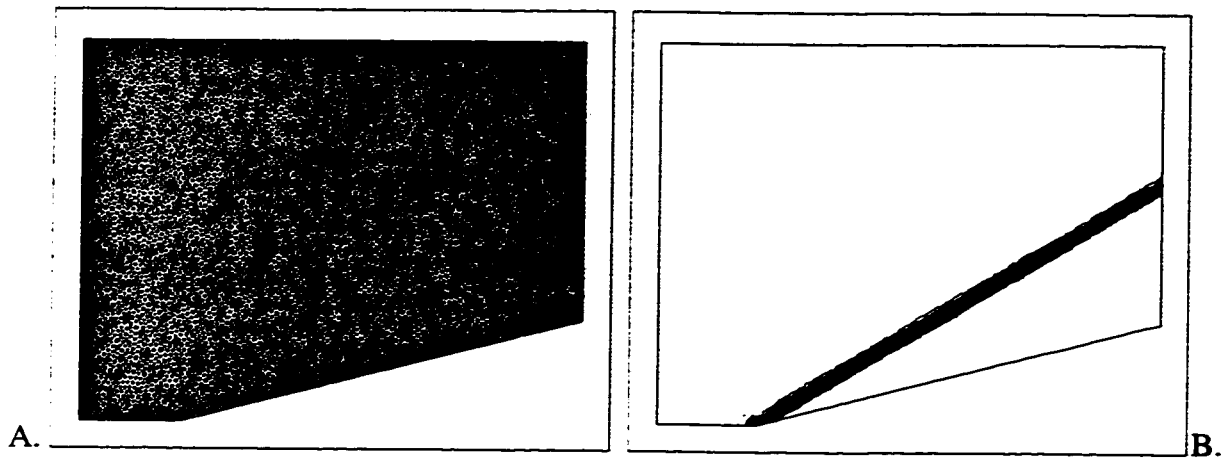

Figure A.1: Initial mesh (A) and the corresponding solution (B) for the supersonic compression corner.

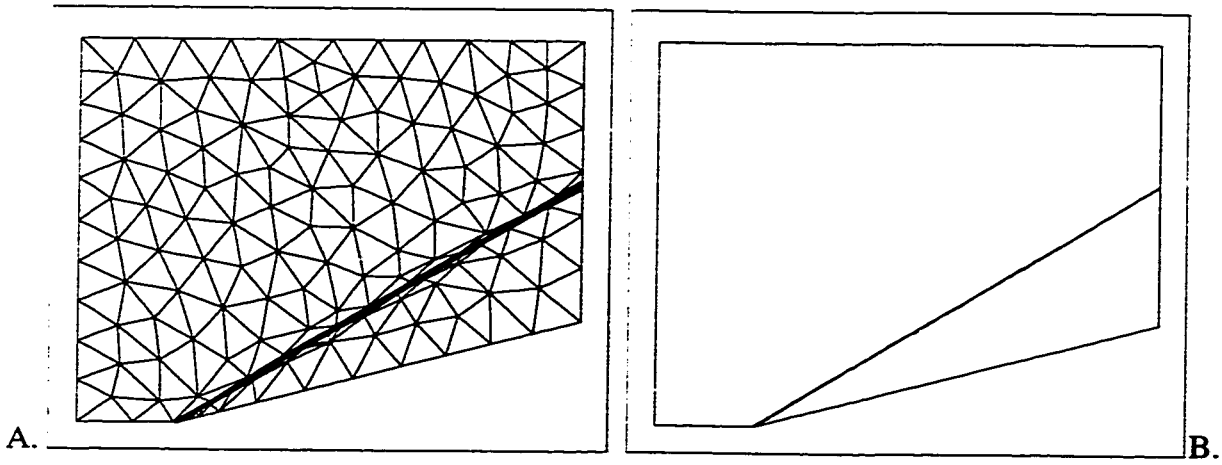

Figure A.2: Adapted mesh (A) and the corresponding solution (B) for the supersonic compression corner.

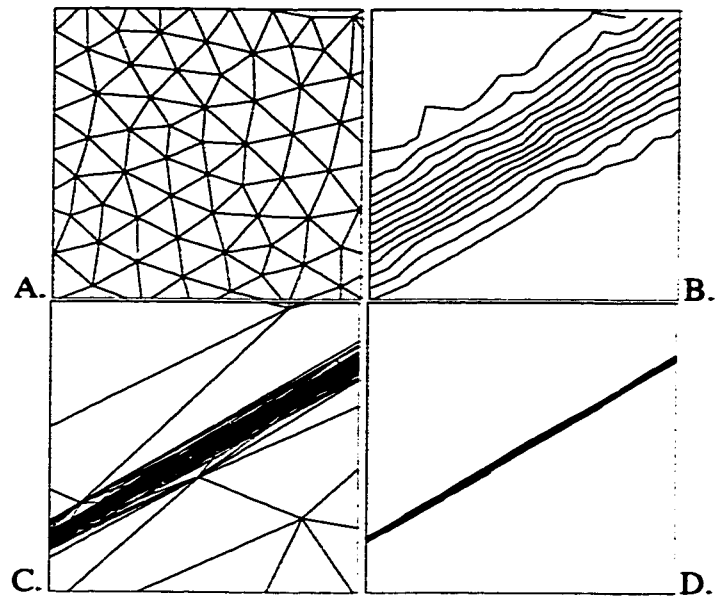

Figure A.3: Close-up view of the shock region on the initial (A) and adapted (C) meshes with the corresponding solutions (B) and (D) for the supersonic compression corner.

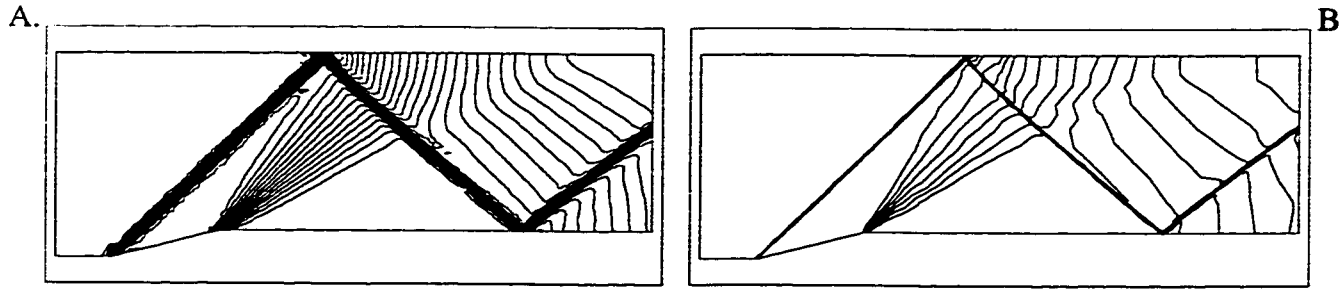

Figure A.4: Iso-Mach lines for the original (A) and the adapted mesh (B) for supersonic wedge (M = 2).

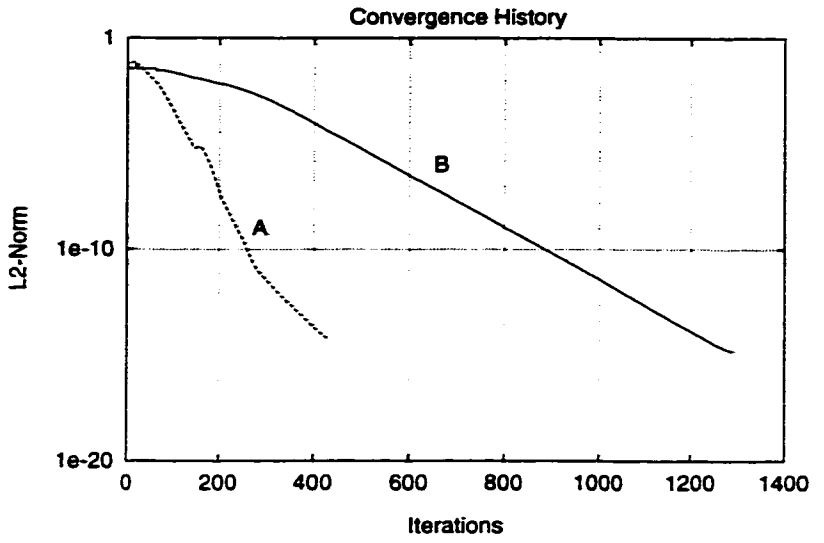

Figure A.5: Convergence history for the supersonic wedge with an inlet Mach number of 2 with (A) and without (B) implicit residual smoothing.

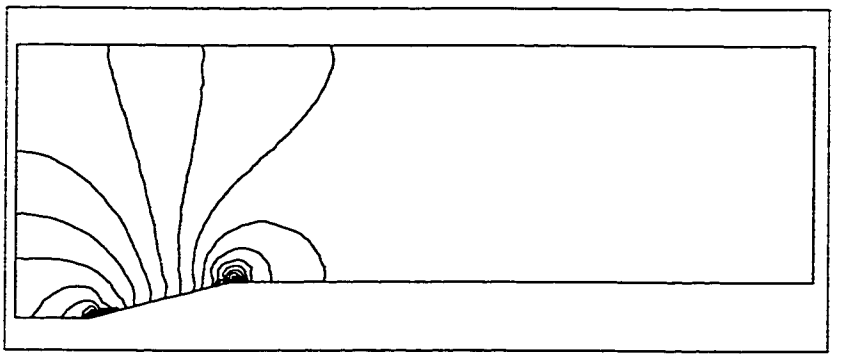

Figure A.6: Iso-Mach lines for subsonic 15° wedge test case.

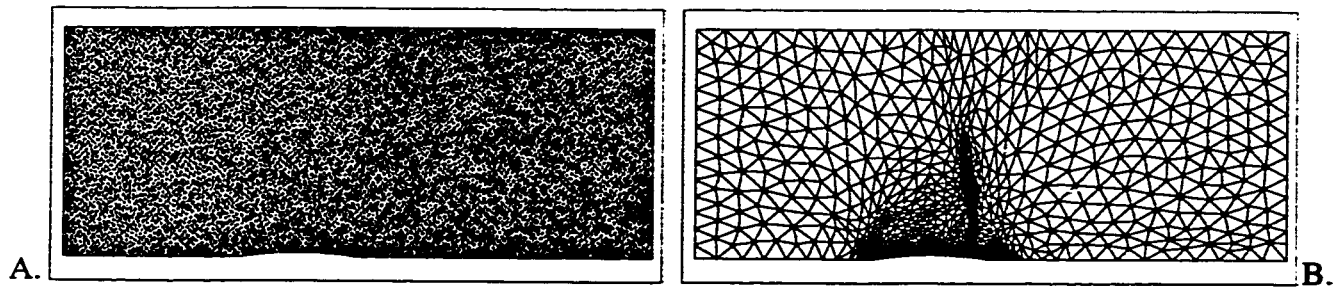

Figure A.7: Initial (A) and the adapted mesh (B) for the transonic bump GAMM-test case.

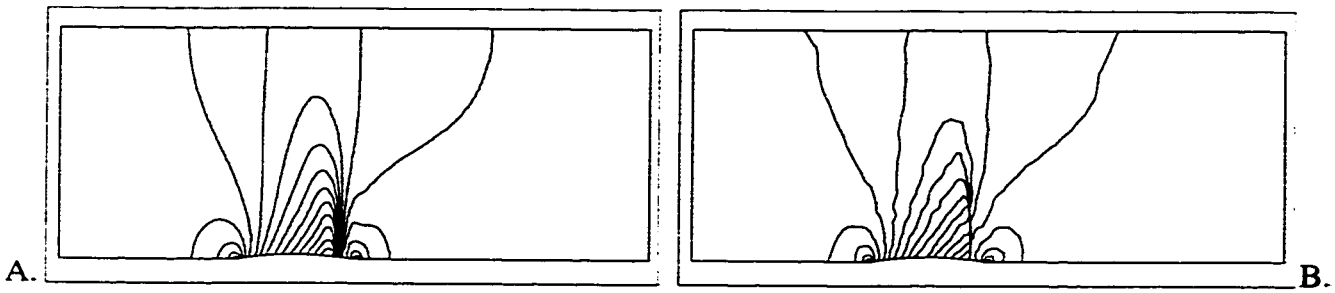

Figure A.8: Iso-Mach lines for the original (A) and the adapted mesh (B) for the transonic bump GAMM-test case.

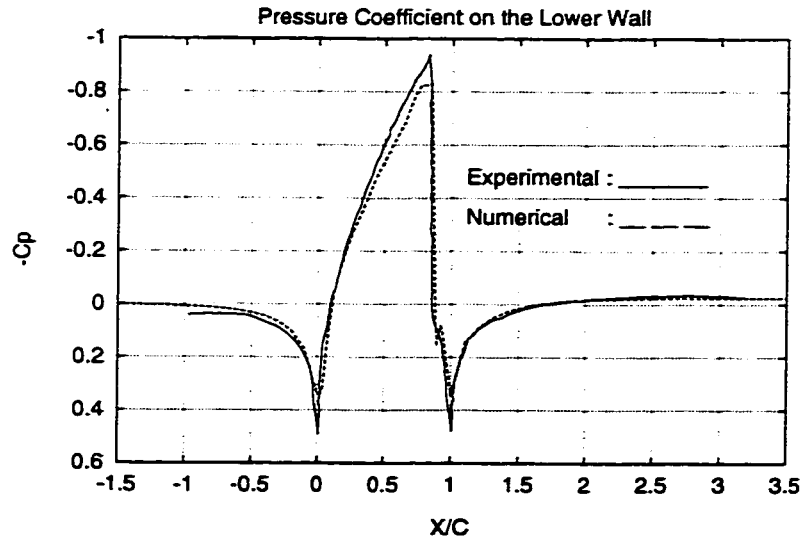

Figure A.9: Computed and experimental values of C_p for transonic GAMM-test case.

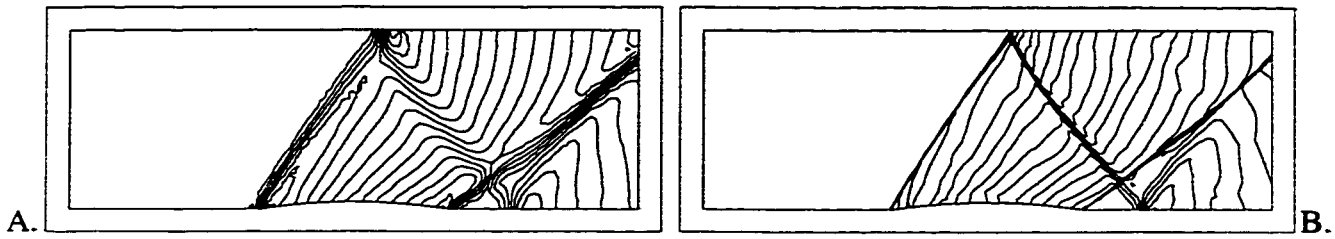

Figure A.10: Iso-Mach lines for the original (A) and the adapted mesh (B) for the supersonic bump ($\mathbf{M = 1.4}$).

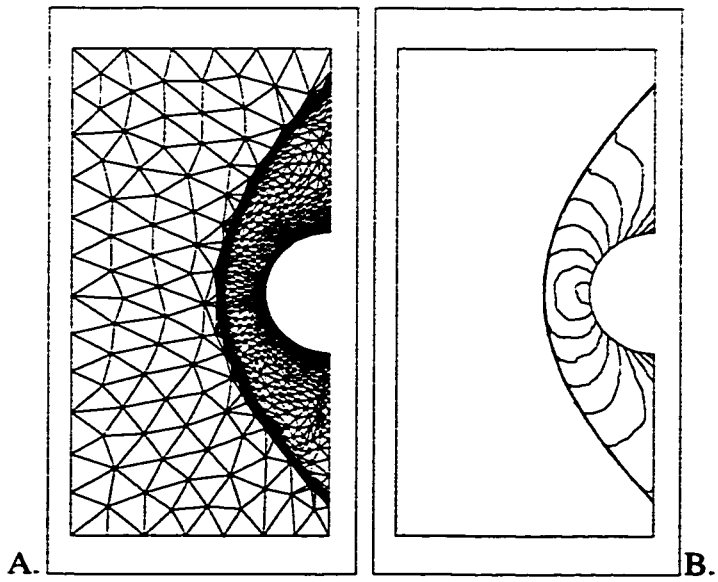

Figure A.11: The anisotropic adapted mesh (A) and solution (B) for supersonic blunt body ($\mathbf{M = 3.0}$).

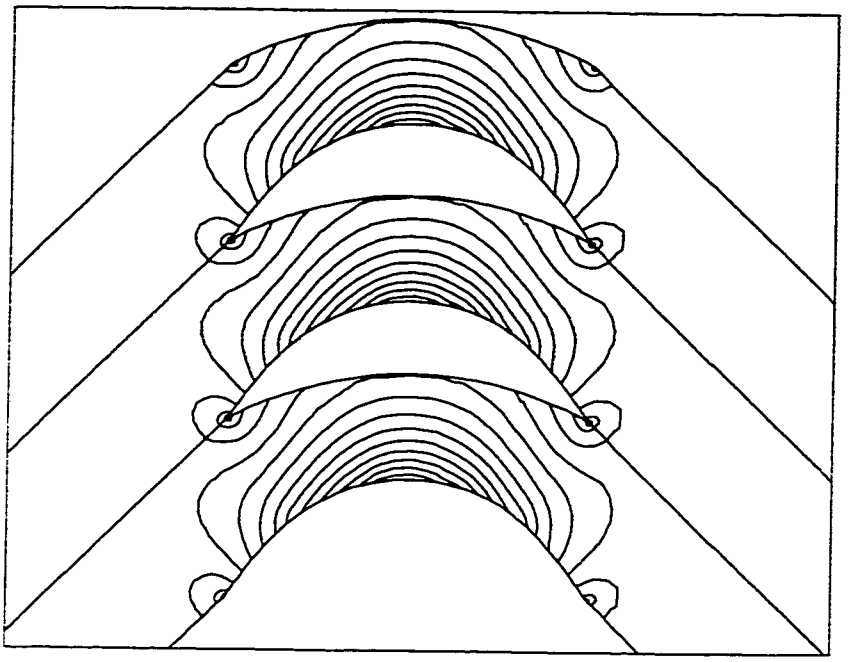

Figure A.12: Iso-Mach lines for Hobson turbine cascade.

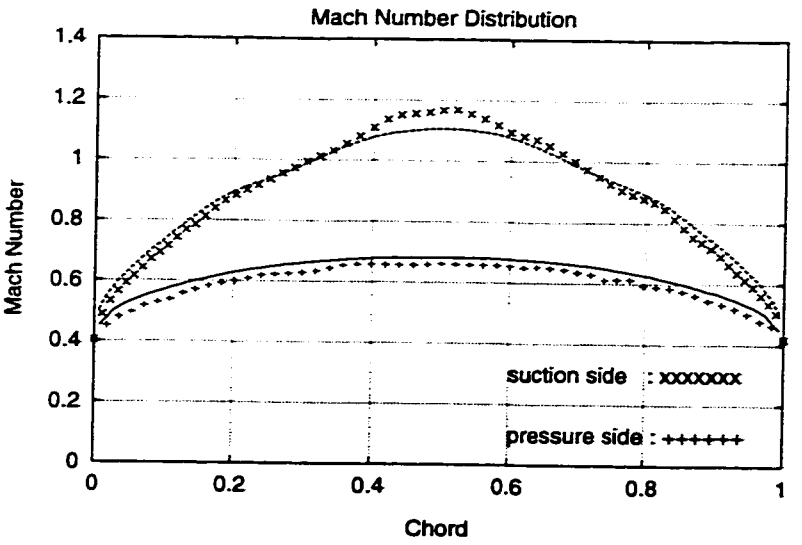

Figure A.13: Computed and Analytical Mach Number Distribution for Hobson's shock-free cascade.

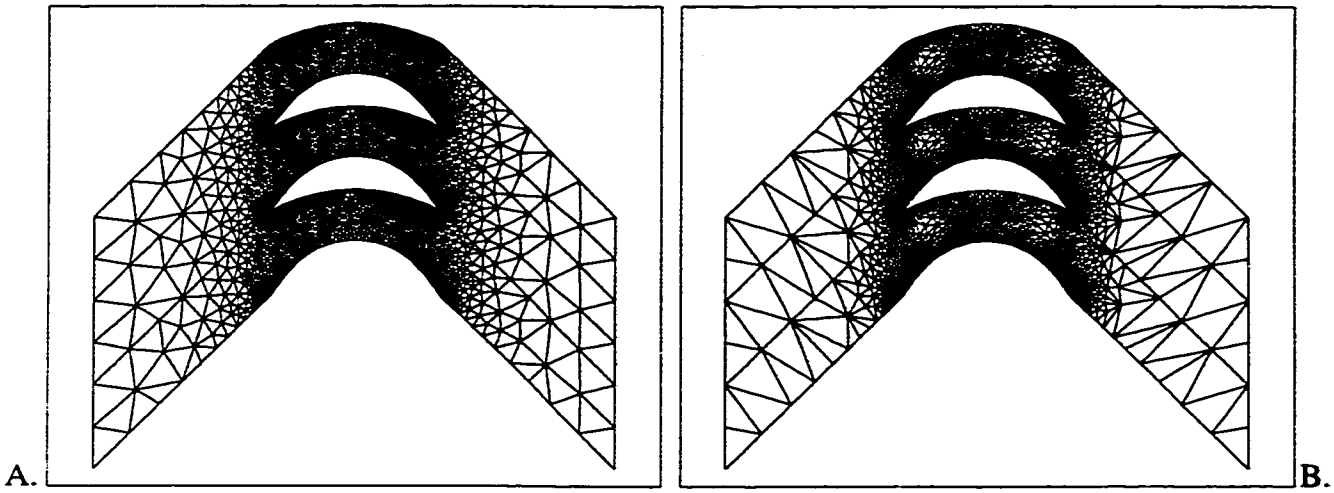

Figure A.14: The original (A) and the adapted mesh (B) for Hobson turbine cascade.

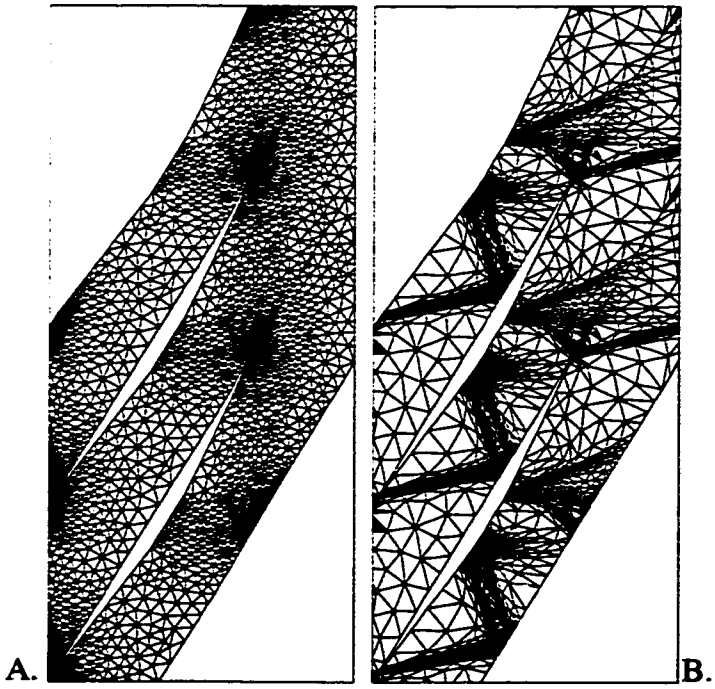

Figure A.15: The original (A) and the adapted mesh (B) for supersonic wedge cascade.

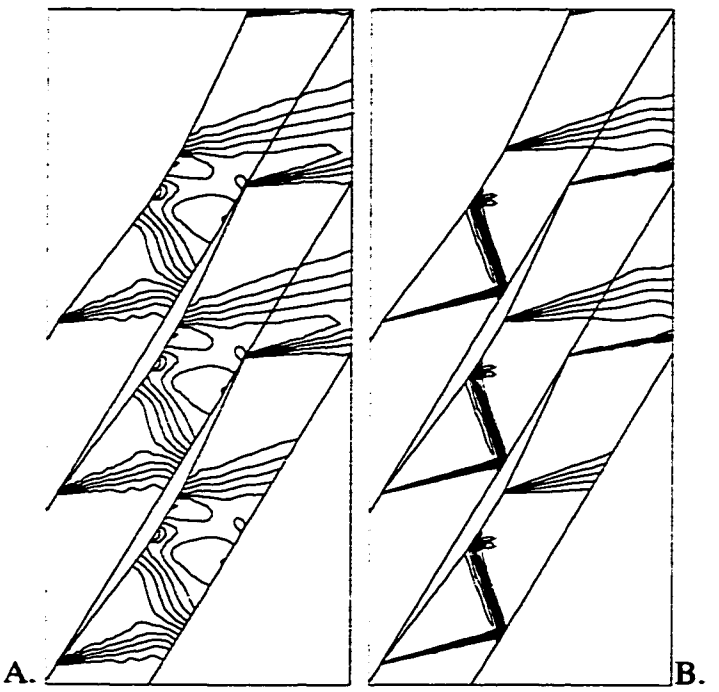

Figure A.16: Iso-Mach lines for the original (A) and the adapted mesh (B) for supersonic wedge cascade.

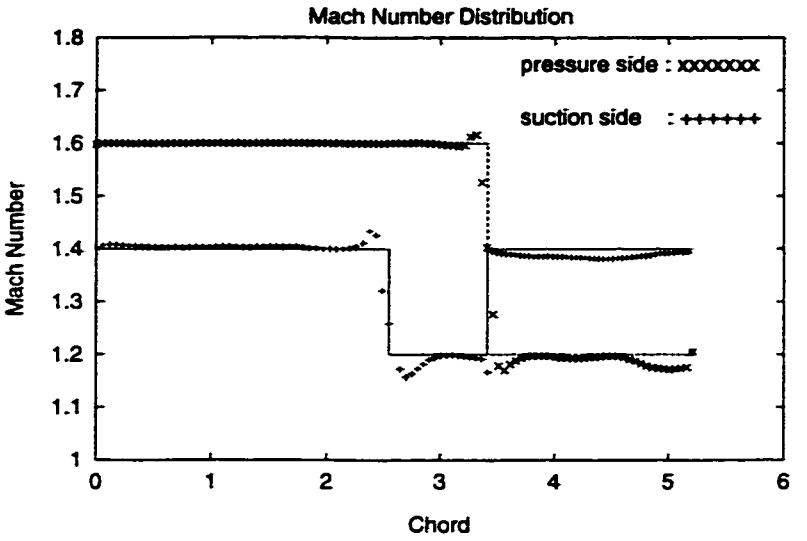

Figure A.17: Computed and Analytical Mach Number Distribution for supersonic wedge cascade.

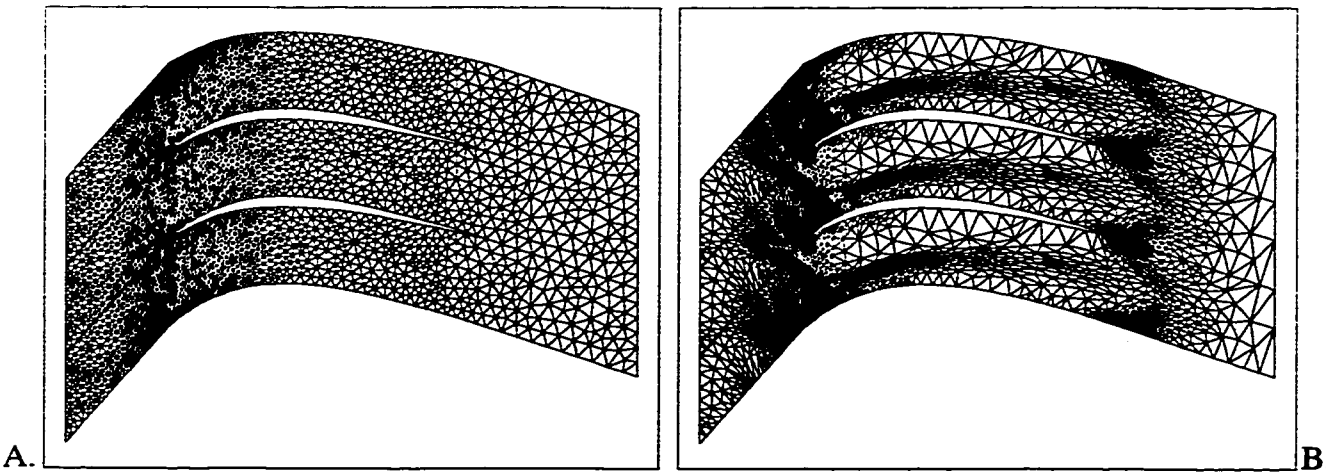

Figure A.18: The original (A) and the anisotropic adapted mesh (B) for ONERA compressor cascade.

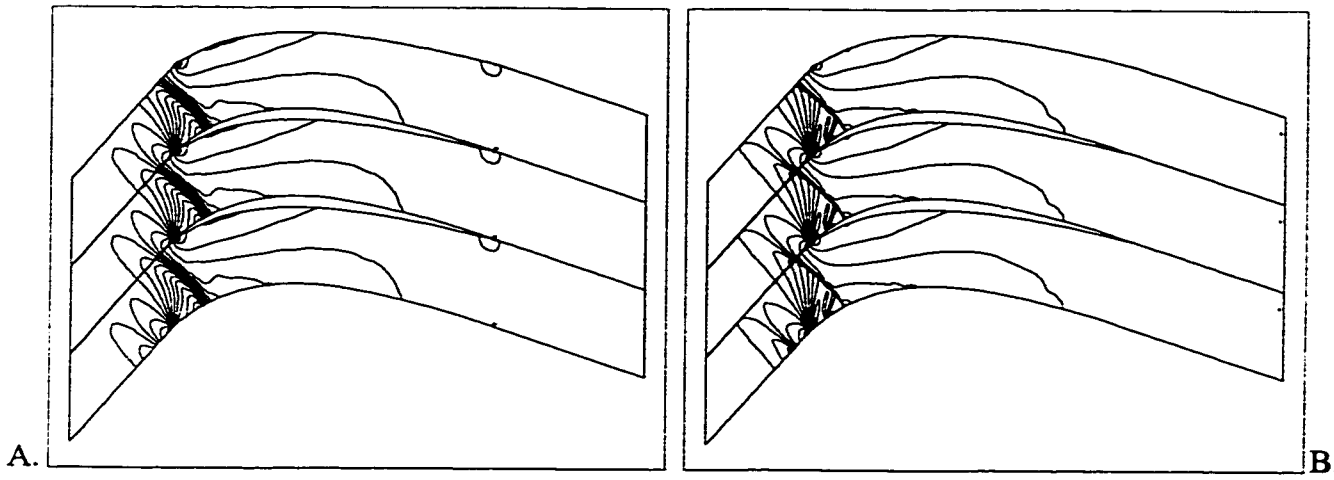

Figure A.19: Iso-Mach lines for the original (A) and the adapted mesh (B) for ONERA compressor cascade.